A plate theory for inflatable panels

Paul Lacorre, Anh Le Van, Rabah Bouzidi, Jean-Christophe Thomas

A plate theory for inflatable panels

Paul Lacorre, Anh Le van, Rabah Bouzidi, Jean-Christophe Thomas*

Nantes Université, École Centrale Nantes, CNRS, GeM, UMR 6183, F-44000 Nantes, France

Abstract

An inflatable panel is an airtight membrane structure whose envelope has two parallel flat sides when pressurized. It acquires load-carrying capacity due to its internal pressure. While pressurized tubes have been studied extensively over the past decades, panels were less investigated. In this work, a model of inflatable panels including shear effects is proposed. The nonlinear equations of motion are derived from the principle of virtual power within the framework of finite deformations and exhibit the essential pressure terms that allow for the correct prediction of the panel behavior. The equations are then linearized around the pre-stressed reference configuration and solved for a simply-supported circular panel subjected to a uniform load. The solution is found to be in good agreement with 3D finite element results.

Keywords: inflatable panel, drop-stitch, pressurized membrane structure, large deformation, linearization, circular plate

https://doi.org/10.1016/j.ijsolstr.2022.111969

Click here to read this article on ScienceDirect.

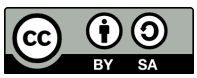

1. Introduction

Inflatable structures are part of membrane tensile structures and they belong to the pneumatic structures category. In such structures, the stiffness comes from the pressurized

*Corresponding author. Tel.: +33251125556

Email address: jean-christophe.thomas@univ-nantes.fr (Jean-Christophe Thomas)

gas they contain which induces pretension in the membranes and provides bearing capacity. Inflatable structures have gained in popularity due to their numerous interesting properties: they are lightweight, reusable, easy to manufacture and to repair, and the inflation level may be adjusted to achieve the desired stiffness. Tensile membrane structures are in rapid development as evidenced by the efforts to guide the structural design of such structures in Europe [1] and thus a theoretical model of inflatable panels is needed.

One of the simplest inflatable structures is the inflatable beam, which is a pressurized tubular membrane whose bearing capacity is entirely due to internal pressure. Although the first study of inflatable panels predated the studies of inflatable beams, pioneering works on inflatable structures started with inflatable beams due to their relatively simple geometry which allows to model them using one-dimensional beam theories. The first studies done by Comer and Levy [2] in 1963, Webber [3] in 1982 and Main et al. [4, 5] in 1994 were based on the Euler-Bernoulli kinematics and were improved by including shear effects with the Timoshenko model in the works of Fichter [6] in 1966, Steeves [7] in 1975, Wielgosz and Thomas [8] in 2002, Le van and Wielgosz [9] in 2005. Then, several studies extended these theories by adding orthotropy and buckling loads of beam-columns with Apedo in 2009 [10], T. T. Nguyen in 2012 [11, 12] and Q. T. Nguyen [13] in 2015. Now that inflatable beams theories are well-established, inflatable plate theory is the logical continuation and thus worth investigating. While the technology of inflatable panels is not new, there are few studies dedicated to them and modeling them correctly is becoming an important issue.

An inflatable panel is a membrane structure whose shape is more complex than an inflatable beam: it is composed of two membranes, namely the upper and lower membranes, which are parallel and of identical shape, and a lateral membrane to seal the panel and ensure airtightness, as well as yarns connecting the upper and lower membranes to maintain a fixed distance between them. This manufacturing technique is called drop-stitch, Fig. 1a. When the structure is pressurized, it has the external shape of a plate.

Inflatable panels were first envisioned as airplane wings by the Goodyear Aircraft Company and also as possible reentry vehicles or heat shields by NASA [14]. As of today, applications of inflatable panels can be seen with floating platforms (Fig. 1b), inflatable movie screens, stand-up paddles and inflatable habitats for space exploration. There are

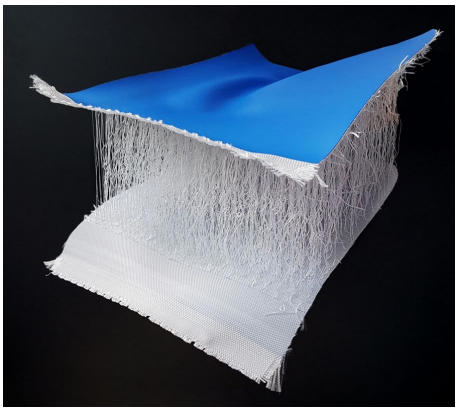

(a) Cut view of drop-stitch fabric exhibiting yarns.

(b) Floating decontamination platform. (© Écocréation)

Figure 1: Internal structure and real-world application of an inflatable panel.

also patents for inflatable wings, antennas, dams and rescue boards.

The pioneering works on inflatable panels date from the '60s. A few technical notes were written at NASA by Leonard, Brooks and McComb [14, 15]. These authors studied rectangular inflatable panels designed by the Goodyear Aircraft Corporation, which they called *airmats*. The first paper by Leonard et al. [14] in 1960 presented a small-deflection theory with elastic orthotropic membranes in Cartesian coordinates. They assumed that the drop-stitch yarns (or drop cords) were inextensible but not necessarily orthogonal to the upper and lower membranes, which allowed for shear deformations in the panel. They pointed out that this theory is a special case of the well-known Reissner-Mindlin theory where the transverse shear stiffness is proportional to the pressurization. One year later, McComb [15] formulated a nonlinear theory with the principle of minimum potential energy and included the effects of a small linear taper. He found solutions in the form of Fourier series for the simply supported and clamped rectangular plates of constant thickness. This theory cannot be applied to circular panels and lacks a pre-stress moment that is obtained in the present paper. A detailed review of the works that followed in the same decade can be found in Habip [16]. Near the end of the 20th century, the research on drop-stitch panels was continued by Kawabata and Ishii [19]. Their paper, which was not translated into English, discusses the effective stiffness of drop-stitch panels when the drop yarns density is low, allowing periodic bulges to form on the top and bottom surfaces. More recently,

Wielgosz and Thomas [8] and Cavallaro [17] took another look at the deflection of inflatable panels by modeling them as inflatable beams. Wielgosz and Thomas [18] also built an inflatable finite element dedicated to inflatable panels, once again modeled using inflatable beam theory. Lately, several studies were conducted at the University of Rhode Island to experimentally determine material parameters and perform finite element simulations on inflatable drop-stitch panels [20, 21, 22]. Davids et al. [23, 24] continued to consider 1D inflatable panel models and conducted experimental and computational studies while including the orthotropic behavior of the membranes, the coupling between shear and moment and the presence of rounded panel edges. They also simulated the post-wrinkling response numerically.

This paper aims to establish a new theoretical foundation for the study of drop-stitch panels. The plan of this article is as follows:

i. The inflatable panel model will incorporate the Reissner-Mindlin kinematics to allow shear deformation. As observed with inflatable beams, the internal pressure plays a critical role in the load-bearing capacity of the structure, which is why the mechanical response cannot be predicted correctly without incorporating pressure terms in the governing equations of inflatable panels. To take this fact into account, the formulation will be done in large deformations, large displacements and large rotations and we choose to derive the governing equations using the principle of virtual power, a simple and systematic method which yields a system of nonlinear equations containing all the pressure terms required for a theory of inflatable panels. All the equations will be given in the tensor form rather than in a particular coordinate systems.

ii. The next part of the paper is concerned with the usual case when the inflatable panel undergoes small displacements and rotations. The linearized equations will be derived from the above-found nonlinear equations, with special emphasis on the treatment of the terms relating to the inflating pressure and the other external loads.

iii. In the last part of the paper, we shall investigate the example of a simply-supported circular inflatable panel undergoing static bending. The analytical solution will be obtained from the linearized theory, with a discussion on its limit of validity corresponding to the onset of the membrane wrinkling. Numerical results obtained from the found so-

lution will be compared with those from a 3D finite element code.

2. Geometry and kinematics

2.1. Reference geometry

The kinematics of the panel is described in a three-dimensional Euclidean space endowed with an orthonormal coordinate system $(\mathbf{O}; \boldsymbol{e}_1, \boldsymbol{e}_2, \boldsymbol{e}_3)$. *The reference configuration* of the panel is the equilibrium *pre-stressed* position Ω_0 where the panel is subjected to the inflating pressure only. It is assumed that, in the reference configuration, the upper and lower membranes are parallel and at equal distance from the plane $(\mathbf{O}; \boldsymbol{e}_1, \boldsymbol{e}_2)$, Fig. 2. The fibers (i.e. the drop-stitch yarns) are vertical, and their density is assumed to be high enough for the membranes to be flat in the reference configuration. The reader is referred to Kawabata and Ishii's paper [19] for more details on the case when the drop yarns density is low, allowing periodic bulges to form on the top and bottom surfaces.

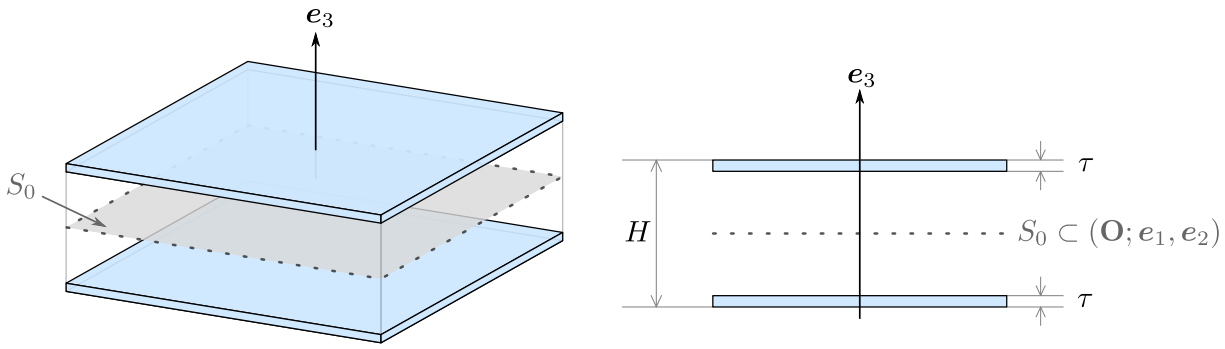

Figure 2: Reference configuration and cross-sectional view of the upper and lower membranes.

In the reference configuration, the mid-surface S_0 is a plane of symmetry of the panel and lies in the plane $(\mathbf{O}; \boldsymbol{e}_1, \boldsymbol{e}_2)$. Any point $\mathbf{P}_0$ on S_0 corresponds to the unique curvilinear coordinates (ξ^1, ξ^2) that lie in a bounded subset of $\mathbb{R}^2$ called the *parameter space* S_ξ, Fig. 3. The local covariant basis vectors on the mid-surface are defined as

$$\forall \alpha \in \{1, 2\}, \quad \boldsymbol{A}_\alpha = \frac{\partial \mathbf{P}_0}{\partial \xi^\alpha}$$

Let τ be the thickness of the membranes in the reference configuration, H the overall thickness of the panel, Fig. 2. The Cartesian coordinates of any point inside the region Ω_0,

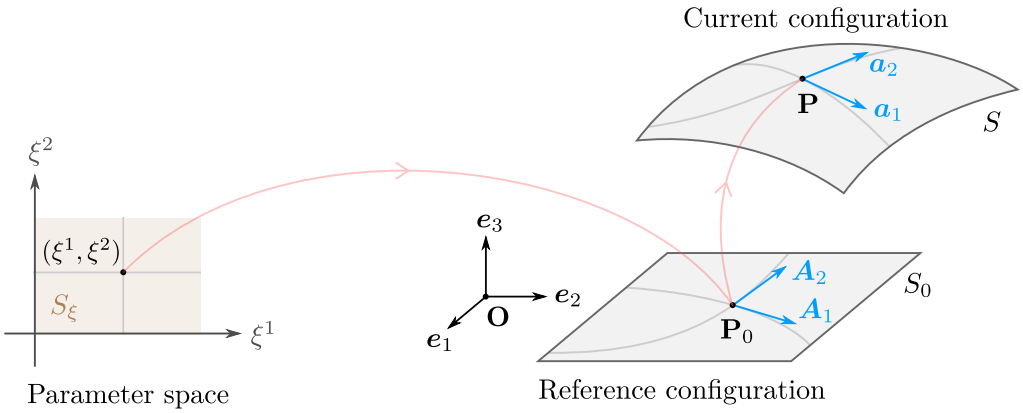

Figure 3: Mid-surface of the panel. The red lines represent the transformations from the parameter space to the reference configuration and from the reference configuration to the current one.

i.e. inside the membranes, are (X, Y, Z), where the coordinate Z belongs to the disconnected interval

$$T = \left[-\frac{H}{2}\ ,\ -\frac{H}{2}+\tau\right] \cup \left[\frac{H}{2}-\tau\ ,\ \frac{H}{2}\right] \tag{1}$$

The reference geometry of the panel can be described by a single equation that maps the parameter space to the physical space. For a triplet of parameters $(\xi^1, \xi^2, \xi^3 \equiv Z) \in S_\xi \times T$, any point $\mathbf{Q}_0$ in Ω_0 is such that $\mathbf{Q}_0 = \mathbf{P}_0(\xi^1, \xi^2) + Z\boldsymbol{e}_3$. The local basis vectors are also defined at any point $\mathbf{Q}_0 \in \Omega_0$:

$$\forall i \in \{1, 2, 3\}, \quad \boldsymbol{G}_i = \frac{\partial \mathbf{Q}_0}{\partial \xi^i} = \boldsymbol{A}_i$$

2.2. Displacement field

The displacement of the panel at time t is defined by the displacement $\boldsymbol{U}(\mathbf{P}_0, t)$ of the mid-surface, which will be denoted $\boldsymbol{U}$ in the sequel, and the director vector $\boldsymbol{a}_3 \equiv \boldsymbol{a}_3(\mathbf{P}_0, t)$, which represents the drop-stitch yarns direction (not necessarily normal to the mid-surface):

$$\boldsymbol{U}(\mathbf{Q}_0, t) = \boldsymbol{U} + Z(\boldsymbol{a}_3 - \boldsymbol{e}_3)$$

The Reissner-Mindlin hypothesis states that the material segments may rotate but not stretch. As a consequence, the vector $\boldsymbol{e}_3$ is transformed into $\boldsymbol{a}_3$ by applying a time-dependent

rotation:

$$\boldsymbol{a}_3 = \boldsymbol{R}(\xi^1, \xi^2, t) \cdot \boldsymbol{e}_3 \tag{2}$$

where $\boldsymbol{R}$ is the rotation tensor. The displacement field $\boldsymbol{U}$ and the director vector field $\boldsymbol{a}_3$ are the unknowns of the problem. The natural covariant basis vectors are expressed in terms of the unknowns of the problem $\boldsymbol{U}$ and $\boldsymbol{a}_3$: $\forall \alpha \in \{1, 2\}$,

$$\forall \mathbf{P} \in S,\ \boldsymbol{a}_\alpha \equiv \frac{\partial \mathbf{P}}{\partial \xi^\alpha} = \boldsymbol{A}_\alpha + \boldsymbol{U}_{,\alpha} \qquad \forall \mathbf{Q} \in \Omega,\ \boldsymbol{g}_\alpha \equiv \frac{\partial \mathbf{Q}}{\partial \xi^\alpha} = \boldsymbol{a}_\alpha + Z\boldsymbol{a}_{3,\alpha} \tag{3}$$

Additionally, $\boldsymbol{g}_3 = \boldsymbol{a}_3$. We also define the coefficients $a_{ij} = \boldsymbol{a}_i \cdot \boldsymbol{a}_j$, $\forall i, j \in \{1, 2, 3\}$. The displacement gradient is

$$\mathbf{grad}_{\mathbf{Q}_0} \boldsymbol{U}(\mathbf{Q}_0, t) = \boldsymbol{U}_{,\alpha} \otimes \boldsymbol{A}^\alpha + (\boldsymbol{a}_3 - \boldsymbol{e}_3) \otimes \boldsymbol{e}_3 + Z\boldsymbol{a}_{3,\alpha} \otimes \boldsymbol{A}^\alpha \tag{4}$$

where $\boldsymbol{A}^\alpha$ is the dual vector of $\boldsymbol{A}_\alpha$ and Einstein summation convention is made from 1 to 2 on Greek indices.

2.3. Green strain tensor

The Green strain tensor $\boldsymbol{E}$ is given by

$$\boldsymbol{E} = E_{ij}\boldsymbol{A}^i \otimes \boldsymbol{A}^j = \frac{1}{2}(g_{ij} - G_{ij})\boldsymbol{A}^i \otimes \boldsymbol{A}^j$$

where $g_{ij} \equiv \boldsymbol{g}_i \cdot \boldsymbol{g}_j$, $G_{ij} = A_{ij} \equiv \boldsymbol{A}_i \cdot \boldsymbol{A}_j$ and Einstein summation convention is made from 1 to 3 on Latin indices. It is found that $E_{\alpha\beta}$ may be written as a second-order polynomial in Z: $\forall \alpha, \beta \in \{1, 2\}$,

$$\begin{aligned} E_{\alpha\beta} &= E^{(0)}_{\alpha\beta} + ZE^{(1)}_{\alpha\beta} + Z^2E^{(2)}_{\alpha\beta} \\ E_{\alpha 3} &= \tfrac{1}{2}a_{\alpha 3} \\ E_{33} &= 0 \end{aligned} \tag{5}$$

where the components $E^{(0)}_{\alpha\beta}$, $E^{(1)}_{\alpha\beta}$, $E^{(2)}_{\alpha\beta}$ are, $\forall \alpha, \beta \in \{1, 2\}$,

$$\begin{aligned} E^{(0)}_{\alpha\beta} &= \tfrac{1}{2}\big(a_{\alpha\beta} - A_{\alpha\beta}\big) \\ E^{(1)}_{\alpha\beta} &= \tfrac{1}{2}\big(\boldsymbol{a}_\alpha \cdot \boldsymbol{a}_{3,\beta} + \boldsymbol{a}_{3,\alpha} \cdot \boldsymbol{a}_\beta\big) \\ E^{(2)}_{\alpha\beta} &= \tfrac{1}{2}\boldsymbol{a}_{3,\alpha} \cdot \boldsymbol{a}_{3,\beta} \end{aligned} \tag{6}$$

3. Equations of motion

3.1. Principle of virtual power

The equations of motion of the inflatable panel will next be obtained using the principle of virtual power, which states that, for any arbitrary virtual velocity field $\boldsymbol{U}^*(\mathbf{Q}_0)$, the sum of the virtual powers of internal forces $\mathcal{P}^*_{\text{int}}$ and external forces $\mathcal{P}^*_{\text{ext}}$ equals the virtual power of inertial quantities $\mathcal{P}^*_{\text{accel}}$:

$$\mathcal{P}^*_{\text{int}} + \underbrace{\mathcal{P}^*_p + \mathcal{P}^*_{\text{ext}\backslash p}}_{\mathcal{P}^*_{ext}} = \mathcal{P}^*_{\text{accel}} \tag{7}$$

In the above expression, $\mathcal{P}^*_{ext}$ is decomposed into two terms: the virtual power due to the inflation pressure $\mathcal{P}^*_p$ and the virtual power of other external loads $\mathcal{P}^*_{\text{ext}\backslash p}$.

3.2. Virtual velocity field

At any point $\mathbf{Q}_0$ of the structure, the virtual velocity field is

$$\boldsymbol{U}^*(\mathbf{Q}_0) = \boldsymbol{U}^* + Z\boldsymbol{a}^*_3 \tag{8}$$

where $\boldsymbol{U}^* \equiv \boldsymbol{U}^*(\mathbf{P}_0)$ is the virtual velocity of the mid-surface and $\boldsymbol{a}^*_3$ the virtual director vector. According to the Reissner-Mindlin kinematics, the fibers do not stretch: they behave as rigid bodies, as shown by the relation $\dot{\boldsymbol{a}}_3 = \boldsymbol{\Omega} \times \boldsymbol{a}_3$ ($\boldsymbol{\Omega}$ is the axial vector of $\dot{\boldsymbol{R}}\boldsymbol{R}^{-1}$ with $\boldsymbol{R}$ the rotation tensor in Relation (2)). For this reason, the virtual director vector is taken of the same form:

$$\boldsymbol{a}^*_3 = \boldsymbol{\omega}^* \times \boldsymbol{a}_3$$

where the virtual rotation velocity vector $\boldsymbol{\omega}^*$ is arbitrary.

3.3. Virtual power of internal forces

The virtual power of internal forces $\mathcal{P}^*_{\text{int}}$ is defined as

$$\mathcal{P}^*_{\text{int}} = -\int_{\Omega_0} \boldsymbol{\Pi}^{\mathsf{T}} : \mathbf{grad}_{\mathbf{Q}_0}\, \boldsymbol{U}^*(\mathbf{Q}_0)\, \mathrm{d}\Omega_0 \tag{9}$$

where $\mathbf{\Pi}$ is the first Piola-Kirchhoff stress tensor and the virtual velocity gradient is calculated using Relation (8):

$$\mathbf{grad}_{\mathbf{Q}_0} \boldsymbol{U}^*(\mathbf{Q}_0) = \boldsymbol{U}^*_{,\alpha} \otimes \boldsymbol{A}^\alpha + \boldsymbol{a}^*_3 \otimes \boldsymbol{e}_3 + Z\boldsymbol{a}^*_{3,\alpha} \otimes \boldsymbol{A}^\alpha \tag{10}$$

In Relation (9), the integral over region Ω_0 of any scalar function $u(\mathbf{Q}_0, t)$ is rewritten using the following standard transformation

$$\int_{\Omega_0} u(\mathbf{Q}_0, t)\,\mathrm{d}\Omega_0 = \int_{S_\xi} \left(\int_T u(\mathbf{Q}_0, t)\,\mathrm{d}Z \right) \sqrt{A}\,\mathrm{d}\xi^1\,\mathrm{d}\xi^2 = \int_{S_0} \left(\int_T u(\mathbf{Q}_0, t)\,\mathrm{d}Z \right) \mathrm{d}S_0$$

in which A is the determinant of the metric tensor. Inserting the expression for the virtual velocity gradient (10) into Relation (9) leads to

$$\mathcal{P}^*_{\text{int}} = -\int_{S_0} \left(\int_T \mathbf{\Pi} \cdot \boldsymbol{A}^\alpha\,\mathrm{d}Z \cdot \boldsymbol{U}^*_{,\alpha} + \int_T Z\mathbf{\Pi} \cdot \boldsymbol{A}^\alpha\,\mathrm{d}Z \cdot \boldsymbol{a}^*_{3,\alpha} + \int_T \mathbf{\Pi} \cdot \boldsymbol{e}_3\,\mathrm{d}Z \cdot \boldsymbol{a}^*_3 \right) \mathrm{d}S_0$$

Let us define the internal forces $\boldsymbol{R}^\alpha$, $\boldsymbol{S}$ and the internal moments $\boldsymbol{L}^\alpha$ as follows: $\forall \alpha \in \{1, 2\}$,

$$\boldsymbol{R}^\alpha = \int_T \mathbf{\Pi} \cdot \boldsymbol{A}^\alpha\,\mathrm{d}Z \qquad \boldsymbol{L}^\alpha = \int_T Z\mathbf{\Pi} \cdot \boldsymbol{A}^\alpha\,\mathrm{d}Z \qquad \boldsymbol{S} = \int_T \mathbf{\Pi} \cdot \boldsymbol{e}_3\,\mathrm{d}Z$$

Then, after integration by parts:

$$\begin{aligned} \mathcal{P}^*_{\text{int}} = &\int_{S_0} \left(\frac{1}{\sqrt{A}} \left(\sqrt{A}\boldsymbol{R}^\alpha \right)_{,\alpha} \cdot \boldsymbol{U}^* + \left(\boldsymbol{a}_3 \times \frac{1}{\sqrt{A}} \left(\sqrt{A}\boldsymbol{L}^\alpha \right)_{,\alpha} - \boldsymbol{a}_3 \times \boldsymbol{S} \right) \cdot \boldsymbol{\omega}^* \right) \mathrm{d}S_0 \\ &- \int_{\partial S_0} \left(\boldsymbol{R}^\alpha \cdot \boldsymbol{U}^* \nu_{0\alpha} + \left(\boldsymbol{a}_3 \times \boldsymbol{L}^\alpha \right) \cdot \boldsymbol{\omega}^* \nu_{0\alpha} \right) \mathrm{d}s_0 \end{aligned} \tag{11}$$

where $\forall \alpha \in \{1, 2\}$, $\nu_{0\alpha} = \boldsymbol{\nu}_0 \cdot \boldsymbol{A}_\alpha$, the vector $\boldsymbol{\nu}_0$ being the outward normal to the edge of the mid-surface ∂S_0. As can be seen later, it is more convenient to work with the so-called

stress resultants $N^{\alpha\beta}$, $M^{\alpha\beta}$, $M^{(2)\alpha\beta}$, Q^{β}, $Q^{(1)\beta}$ defined as: $\forall \alpha, \beta \in \{1,2\}$,

$$\begin{aligned} N^{\alpha\beta} &= \int_T \Sigma^{\alpha\beta}\,\mathrm{d}Z \\ M^{\alpha\beta} &= \int_T Z\Sigma^{\alpha\beta}\,\mathrm{d}Z \qquad & M^{(2)\alpha\beta} &= \int_T Z^2\Sigma^{\alpha\beta}\,\mathrm{d}Z \\ Q^{\beta} &= \int_T \Sigma^{3\beta}\,\mathrm{d}Z \qquad & Q^{(1)\beta} &= \int_T Z\Sigma^{3\beta}\,\mathrm{d}Z \end{aligned} \tag{12}$$

where the components Σ^{ij}, $\forall i,j \in \{1,2,3\}$, of the second Piola-Kirchhoff stress tensor $\boldsymbol{\Sigma} = \Sigma^{ij}\boldsymbol{A}_i \otimes \boldsymbol{A}_j$ are related to those of the first Piola-Kirchhoff stress tensor $\boldsymbol{\Pi}$ by $\Sigma^{ij}\boldsymbol{g}_i = \Pi^{ij}\boldsymbol{G}_i$. The stress resultants $N^{\alpha\beta}$ are called the membrane forces, $M^{\alpha\beta}$ the bending moments, $M^{(2)\alpha\beta}$ the bending moments of order 2, Q^{β} the shear forces and $Q^{(1)\beta}$ the shear forces of order 1. Using also Eq. (3), the internal forces $\boldsymbol{R}^{\alpha}$, $\boldsymbol{L}^{\alpha}$ and $\boldsymbol{S}$ can be written as: $\forall \beta \in \{1,2\}$,

$$\begin{aligned} \boldsymbol{R}^{\beta} &= N^{\alpha\beta}\boldsymbol{a}_{\alpha} + Q^{\beta}\boldsymbol{a}_3 + M^{\alpha\beta}\boldsymbol{a}_{3,\alpha} \\ \boldsymbol{L}^{\beta} &= M^{\alpha\beta}\boldsymbol{a}_{\alpha} + Q^{(1)\beta}\boldsymbol{a}_3 + M^{(2)\alpha\beta}\boldsymbol{a}_{3,\alpha} \\ \boldsymbol{S} &= Q^{\alpha}\boldsymbol{a}_{\alpha} + Q^{(1)\alpha}\boldsymbol{a}_{3,\alpha} + \int_T \Sigma^{33}\,\mathrm{d}Z\boldsymbol{a}_3 \end{aligned} \tag{13}$$

3.4. Virtual power of external forces other than the inflating pressure

It is assumed that there are external forces other than the inflating pressure, which can be represented as forces and torques exerted on the mid-surface, namely the surface force $\boldsymbol{q}$ distributed over S_0 and the line force $\boldsymbol{q}'$ and line torque $\boldsymbol{\Gamma}$ on the edge ∂S_0, Fig. 4. The torque is decomposed into $\boldsymbol{\Gamma} = \Gamma^{\nu}\boldsymbol{\nu} + \Gamma^{s}\boldsymbol{s}$ along the outward normal vector $\boldsymbol{\nu}$ to the edge and the tangent vector $\boldsymbol{s}$ to the edge.

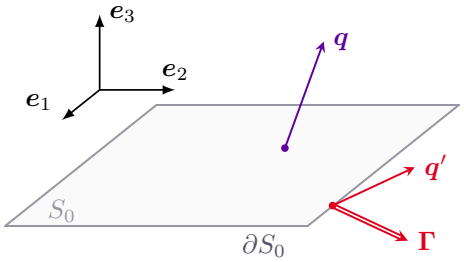

Figure 4: External forces acting on the panel.

The virtual power of external forces other than the inflating pressure is

$$\mathcal{P}^*_{\text{ext}\backslash p} = \int_{S_0} \boldsymbol{q} \cdot \boldsymbol{U}^* \, \mathrm{d}S_0 + \int_{\partial S_0} \left[\boldsymbol{q}' \cdot \boldsymbol{U}^* + \boldsymbol{\Gamma} \cdot \boldsymbol{\omega}^* \right] \mathrm{d}s_0 \tag{14}$$

3.5. Virtual power of the inflating pressure

The panel is inflated with air at a prescribed pressure p which exerts a follower force on the inner surface S_p of the panel in the current configuration. Let S_{0p}, the surface in the reference configuration corresponding to S_p, be partitioned into three parts – S_{0p}^{sup}, S_{0p}^{inf} and S_{0p}^{edge} – as shown in Fig. 5:

- S_{0p}^{sup} and S_{0p}^{inf} are the lower side of the upper membrane and the upper side of the lower membrane, respectively.
- S_{0p}^{edge} is the inner side of the lateral membrane.

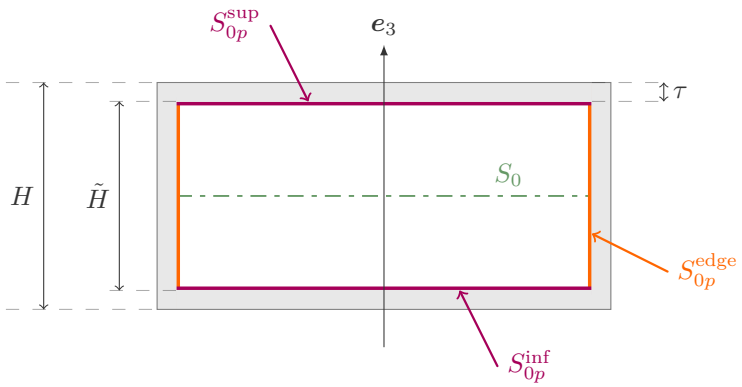

Figure 5: Definition of the surfaces on which the pressure is exerted.

The reference surfaces S_{0p}^{sup}, S_{0p}^{inf}, S_{0p}^{edge} become S_p^{sup}, S_p^{inf} and S_p^{edge}, respectively, in the current configuration. The distance between S_{0p}^{sup} and S_{0p}^{inf} is constant and equals $\tilde{H} = H - 2\tau$. The virtual power of the internal prescribed pressure p is

$$\mathcal{P}^*_p = \int_{S_p} p\boldsymbol{n} \cdot \boldsymbol{U}^*(\mathbf{Q}_0) \, \mathrm{d}S$$

where $\boldsymbol{n}$ is the outward normal vector to the membrane, Fig. 6.

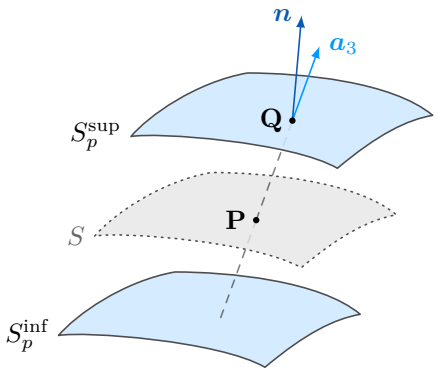

Figure 6: The surfaces S_p^{sup} and S_p^{inf} and the outward normal vector $\boldsymbol{n}$ at point $\mathbf{Q}$ on S_p^{sup}.

The virtual power of pressure forces is split into two terms, the integral $\mathcal{P}^*_{p\to S_p^{\text{sup}}\cup S_p^{\text{inf}}}$ over the upper and lower surfaces and the integral $\mathcal{P}^*_{p\to S_p^{\text{edge}}}$ over the lateral walls:

$$\mathcal{P}^*_p = \mathcal{P}^*_{p\to S_p^{\text{sup}}\cup S_p^{\text{inf}}} + \mathcal{P}^*_{p\to S_p^{\text{edge}}}$$

Pressure over the upper and lower faces.

Let us first consider the virtual power of the pressure exerted on the upper surface:

$$\mathcal{P}^*_{p\to S_p^{\text{sup}}} = \int_{S_p^{\text{sup}}} p\boldsymbol{n}\cdot\boldsymbol{U}^*(\mathbf{Q}_0)\,\mathrm{d}S \tag{15}$$

Similarly to the mid-surface S, the upper surface S_p^{sup} is parametrized by (ξ^1,ξ^2):

$$\begin{array}{ccc} S_\xi & \longrightarrow & S_p^{\text{sup}} \\ (\xi^1,\xi^2) & \mapsto & \mathbf{Q}(\xi^1,\xi^2,t) = \mathbf{P}(\xi^1,\xi^2,t) + \dfrac{\tilde{H}}{2}\boldsymbol{a}_3(\xi^1,\xi^2,t) \end{array}$$

The above expression involves the height $\tilde{H}$ over which the pressure is exerted on the lateral walls, rather than the total height H of the panel. The distinction between $\tilde{H}$ and H will prove to have a noticeable impact on the numerical results.

The natural vectors at a point $\mathbf{Q}$ on the upper surface S_p^{sup} are

$$\forall\alpha\in\{1,2\},\quad \boldsymbol{g}_\alpha = \frac{\partial\mathbf{Q}}{\partial\xi^\alpha} = \boldsymbol{a}_\alpha + \frac{\tilde{H}}{2}\boldsymbol{a}_{3,\alpha} \tag{16}$$

Since the surface element in Relation (15) is $\boldsymbol{n}\,\mathrm{d}S = \boldsymbol{g}_1 \times \boldsymbol{g}_2\,\mathrm{d}\xi^1\,\mathrm{d}\xi^2$, the virtual power of the pressure on the upper surface writes

$$\mathcal{P}^*_{p\to S_p^{\mathrm{sup}}} = p\int_{S_\xi} \boldsymbol{U}^*(\mathbf{Q}_0)\cdot(\boldsymbol{g}_1\times\boldsymbol{g}_2)\,\mathrm{d}\xi^1\,\mathrm{d}\xi^2$$

Moreover, Relation (8) leads to $\boldsymbol{U}^*(\mathbf{Q}_0) = \boldsymbol{U}^* + \boldsymbol{\omega}^* \times \dfrac{\tilde{H}}{2}\boldsymbol{a}_3$ so that Relation (16) becomes

$$\boldsymbol{g}_1\times\boldsymbol{g}_2 = \boldsymbol{a}_1\times\boldsymbol{a}_2 + \frac{\tilde{H}}{2}\left(\boldsymbol{a}_1\times\boldsymbol{a}_{3,2} + \boldsymbol{a}_{3,1}\times\boldsymbol{a}_2\right) + \frac{\tilde{H}^2}{4}\boldsymbol{a}_{3,1}\times\boldsymbol{a}_{3,2}$$

Since $\|\boldsymbol{a}_3\| = 1$, the virtual power of pressure forces acting upon the upper surface is finally

$$\begin{aligned}\mathcal{P}^*_{p\to S_p^{\mathrm{sup}}} = p\int_{S_\xi}\Bigg\{&\boldsymbol{U}^*\cdot(\boldsymbol{a}_1\times\boldsymbol{a}_2) + \boldsymbol{U}^*\cdot\frac{\tilde{H}}{2}\left(\boldsymbol{a}_1\times\boldsymbol{a}_{3,2}+\boldsymbol{a}_{3,1}\times\boldsymbol{a}_2\right) + \boldsymbol{U}^*\cdot\frac{\tilde{H}^2}{4}\boldsymbol{a}_{3,1}\times\boldsymbol{a}_{3,2}\\ &+\boldsymbol{\omega}^*\cdot\frac{\tilde{H}}{2}\boldsymbol{a}_3\times(\boldsymbol{a}_1\times\boldsymbol{a}_2) + \boldsymbol{\omega}^*\cdot\frac{\tilde{H}^2}{4}\boldsymbol{a}_3\times\left(\boldsymbol{a}_1\times\boldsymbol{a}_{3,2}+\boldsymbol{a}_{3,1}\times\boldsymbol{a}_2\right)\Bigg\}\,\mathrm{d}\xi^1\,\mathrm{d}\xi^2 \quad (17)\end{aligned}$$

The same procedure is applied to the lower face S_p^{inf}, with

$$\forall\alpha\in\{1,2\},\quad \boldsymbol{g}_\alpha = \frac{\partial\mathbf{Q}}{\partial\xi^\alpha} = \boldsymbol{a}_\alpha - \frac{\tilde{H}}{2}\boldsymbol{a}_{3,\alpha}$$

and the surface element $\boldsymbol{n}\,\mathrm{d}S = -\boldsymbol{g}_1\times\boldsymbol{g}_2\,\mathrm{d}\xi^1\,\mathrm{d}\xi^2$. The negative sign indicates that the normal to the lower membrane faces downwards. Hence

$$\begin{aligned}\mathcal{P}^*_{p\to S_p^{\mathrm{inf}}} = -p\int_{S_\xi}\Bigg\{&\boldsymbol{U}^*\cdot(\boldsymbol{a}_1\times\boldsymbol{a}_2) - \boldsymbol{U}^*\cdot\frac{\tilde{H}}{2}\left(\boldsymbol{a}_1\times\boldsymbol{a}_{3,2}+\boldsymbol{a}_{3,1}\times\boldsymbol{a}_2\right) + \boldsymbol{U}^*\cdot\frac{\tilde{H}^2}{4}\boldsymbol{a}_{3,1}\times\boldsymbol{a}_{3,2}\\ &-\boldsymbol{\omega}^*\cdot\frac{\tilde{H}}{2}\boldsymbol{a}_3\times(\boldsymbol{a}_1\times\boldsymbol{a}_2) + \boldsymbol{\omega}^*\cdot\frac{\tilde{H}^2}{4}\boldsymbol{a}_3\times\left(\boldsymbol{a}_1\times\boldsymbol{a}_{3,2}+\boldsymbol{a}_{3,1}\times\boldsymbol{a}_2\right)\Bigg\}\,\mathrm{d}\xi^1\,\mathrm{d}\xi^2 \quad (18)\end{aligned}$$

By summing Relation (17) and Relation (18), the virtual power of pressure forces acting on the upper and lower surfaces of the panel can be expressed as an integral over the reference

mid-surface S_0:

$$\mathcal{P}^*_{p\to S_p^{\sup}\cup S_p^{\inf}} = \int_{S_0} \frac{p\tilde{H}}{\sqrt{A}} (\boldsymbol{a}_1 \times \boldsymbol{a}_{3,2} + \boldsymbol{a}_{3,1} \times \boldsymbol{a}_2)\cdot\boldsymbol{U}^* \,\mathrm{d}S_0 + \int_{S_0} \frac{p\tilde{H}}{\sqrt{A}} \big[\boldsymbol{a}_3 \times (\boldsymbol{a}_1 \times \boldsymbol{a}_2)\big]\cdot\boldsymbol{\omega}^* \,\mathrm{d}S_0 \quad (19)$$

Pressure over the lateral wall.

The internal pressure also acts on the lateral wall S_p^{edge}. The following parametrization is introduced to define the border of the mid-surfaces S_0 and S (Fig. 7):

$$\begin{array}{ccccc} \Lambda & \longrightarrow & \partial S_0 & \longrightarrow & \partial S \\ \lambda & \mapsto & \mathbf{P}_0(\lambda) & \mapsto & \mathbf{P}(\lambda) = \mathbf{P}_0(\lambda) + \boldsymbol{U}(\mathbf{P}_0, t) \end{array}$$

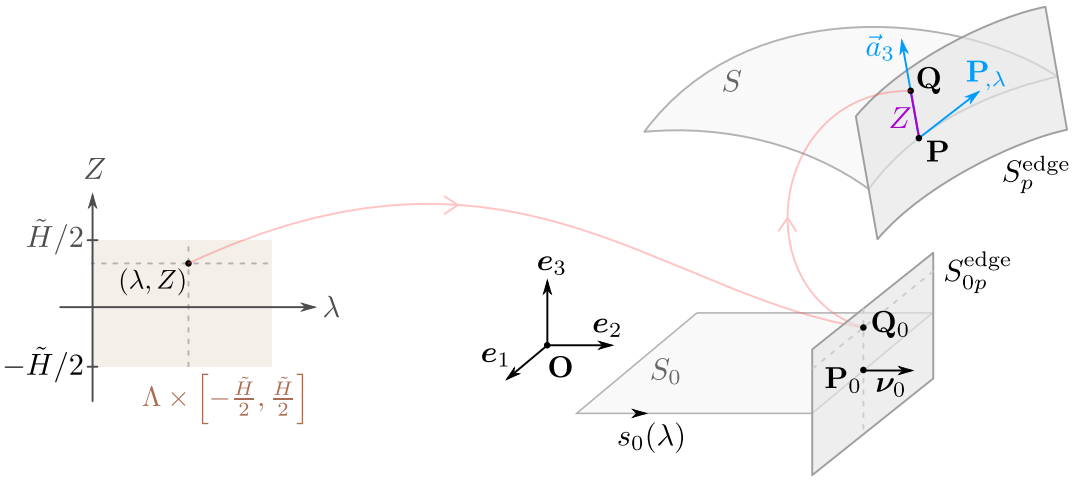

Figure 7: Parametrization of the border in the reference and current configurations. The red lines represent the transformations from the parameter space to the reference configuration and from the reference configuration to the current one.

The following parametrization defines the edge of the plate:

$$\begin{array}{ccc} \Lambda \times \left[-\dfrac{\tilde{H}}{2}, \dfrac{\tilde{H}}{2}\right] & \longrightarrow & S_p^{\text{edge}} \\ (\lambda, Z) & \mapsto & \mathbf{Q}(\lambda, Z) = \mathbf{P}(\lambda) + Z\boldsymbol{a}_3(\lambda) \end{array} \quad (20)$$

In writing this, it is assumed that the material segments of the edges remain straight (Fig. 7), thus ignoring the bulge that may form along the edge of the panel after inflation.

The virtual power of the pressure on the lateral wall is recast in terms of parameters (λ, Z) as

$$\mathcal{P}^*_{p\to S_p^{\text{edge}}} = \int_{S_p^{\text{edge}}} p\boldsymbol{n}\cdot\boldsymbol{U}^*(\mathbf{Q}_0)\,\mathrm{d}S = \int_{\Lambda\times\left[-\frac{\tilde{H}}{2},\frac{\tilde{H}}{2}\right]} \boldsymbol{U}^*(\mathbf{Q}_0)\cdot(\mathbf{Q}_{,\lambda}\times\mathbf{Q}_{,Z})\,\mathrm{d}\lambda\,\mathrm{d}Z \tag{21}$$

On account of the parametrization (20) of the border, the cross product $\mathbf{Q}_{,\lambda}\times\mathbf{Q}_{,Z}$ is

$$\mathbf{Q}_{,\lambda}\times\mathbf{Q}_{,Z} = \mathbf{P}_{,\lambda}\times\boldsymbol{a}_3 + Z\boldsymbol{a}_{3,\lambda}\times\boldsymbol{a}_3$$

Given the expression of the virtual velocity field, $\boldsymbol{U}^*(\mathbf{Q}_0) = \boldsymbol{U}^* + \boldsymbol{\omega}^*\times Z\boldsymbol{a}_3$, the integrand in Relation (21) becomes

$$\boldsymbol{U}^*(\mathbf{Q}_0)\cdot(\mathbf{Q}_{,\lambda}\times\mathbf{Q}_{,Z}) = \boldsymbol{U}^*\cdot\left(\mathbf{P}_{,\lambda}\times\boldsymbol{a}_3 + Z\boldsymbol{a}_{3,\lambda}\times\boldsymbol{a}_3\right) + \boldsymbol{\omega}^*\cdot\left[Z\boldsymbol{a}_3\times(\mathbf{P}_{,\lambda}\times\boldsymbol{a}_3 + Z\boldsymbol{a}_{3,\lambda}\times\boldsymbol{a}_3)\right]$$

In the right-hand side, the virtual quantities $\boldsymbol{U}^*$ and $\boldsymbol{\omega}^*$ are functions of point $\mathbf{P}_0\in S_0$ only. The terms $\mathbf{P}_{,\lambda}$, $\boldsymbol{a}_3$ and $\boldsymbol{a}_{3,\lambda}$ depend solely on λ. Integrating over Z gives the virtual power of the pressure forces on the lateral wall of the panel:

$$\mathcal{P}^*_{p\to S_p^{\text{edge}}} = p\tilde{H}\int_\Lambda \boldsymbol{U}^*\cdot(\mathbf{P}_{,\lambda}\times\boldsymbol{a}_3)\,\mathrm{d}\lambda + \frac{p\tilde{H}^3}{12}\int_\Lambda \boldsymbol{\omega}^*\cdot\boldsymbol{a}_{3,\lambda}\,\mathrm{d}\lambda \tag{22}$$

The total virtual power of the pressure forces $\mathcal{P}^*_p$ is simply the sum of (19) and (22).

Throughout the foregoing, we have assumed that the inflating pressure p is prescribed, possibly as a function of time. In practice, most of inflatable structures are first pressurized using a definite amount of gas and then made airtight. Under these conditions, the pressure p in the internal gas varies as a function of the deformation of the structure. Given the initial state of the gas (volume, pressure, temperature, etc.), one then has to solve a fluid-structure interaction problem so as to capture the increase in p due to the volume reduction. That is a difficult problem which is beyond the scope of our work. In this paper, the internal pressure is assumed to be independent of the interior volume of the inflatable panel, even in finite deformations of the panel.

3.6. Virtual power of inertial forces

The virtual power of the inertial quantity in Eq. (7) is

$$\mathcal{P}^*_{\text{accel}} = \int_{\Omega_0} \rho \ddot{\boldsymbol{U}}(\mathbf{Q}_0, t) \cdot \boldsymbol{U}^*(\mathbf{Q}_0)\, \mathrm{d}\Omega_0$$

where ρ is the density of the membrane (measured in the reference state) and $\ddot{\boldsymbol{U}}(\mathbf{Q}_0, t)$ is the acceleration at point $\mathbf{Q}_0$. Since the membranes are very thin, the density ρ can be assumed uniform through the thickness. The above integral can be transformed into

$$\begin{aligned}\mathcal{P}^*_{\text{accel}} = \int_{S_0} \rho \Bigg(& \ddot{\boldsymbol{U}} \cdot \boldsymbol{U}^* \int_T \mathrm{d}Z + \ddot{\boldsymbol{a}}_3 \cdot \boldsymbol{U}^* \int_T Z\, \mathrm{d}Z \\ & + (\boldsymbol{a}_3 \times \ddot{\boldsymbol{U}}) \cdot \boldsymbol{\omega}^* \int_T Z\, \mathrm{d}Z + (\boldsymbol{a}_3 \times \ddot{\boldsymbol{a}}_3) \cdot \boldsymbol{\omega}^* \int_T Z^2\, \mathrm{d}Z \Bigg)\, \mathrm{d}S_0\end{aligned}$$

where $\ddot{\boldsymbol{a}}_3$ is the second derivative of the director vector $\boldsymbol{a}_3(\mathbf{P}_0, t)$ with respect to time. The integrals carried out over interval T (defined in (1)) are

$$\int_T \mathrm{d}Z = 2\tau \qquad \int_T Z\, \mathrm{d}Z = 0 \qquad \int_T Z^2\, \mathrm{d}Z = \frac{H^3 - (H - 2\tau)^3}{12} = \frac{\tilde{\tau} H^2}{2}$$

where use has been made of the notation $\tilde{\tau} = \left(1 - \dfrac{2\tau}{H} + \dfrac{4\tau^2}{3H^2}\right)\tau$. The virtual power of inertial forces thus becomes

$$\mathcal{P}^*_{\text{accel}} = \int_{S_0} \left(2\tau\rho \ddot{\boldsymbol{U}} \cdot \boldsymbol{U}^* + \frac{\rho \tilde{\tau} H^2}{2} (\boldsymbol{a}_3 \times \ddot{\boldsymbol{a}}_3) \cdot \boldsymbol{\omega}^* \right) \mathrm{d}S_0 \tag{23}$$

3.7. System of nonlinear equations of motion

The final expression of the principle of virtual power (7) is obtained by summing the expressions (11), (14), (19), (22), and (23). For the sake of clarity, let us state the resulting governing equations before proving them.

- **The equations of motion** for the inflatable panel is: $\forall t$, $\forall \mathbf{P}_0 \in S_0$,

$$\frac{1}{\sqrt{A}}\left(\sqrt{A}\boldsymbol{R}^{\alpha}\right)_{,\alpha} + \boldsymbol{q} + \frac{p\tilde{H}}{\sqrt{A}}\left(\boldsymbol{a}_{3,1}\times\boldsymbol{a}_2 + \boldsymbol{a}_1\times\boldsymbol{a}_{3,2}\right) = 2\tau\rho\ddot{\boldsymbol{U}} \tag{24a}$$

$$\frac{1}{\sqrt{A}}\left(\sqrt{A}\boldsymbol{a}_3\times\boldsymbol{L}^{\alpha}\right)_{,\alpha} + \boldsymbol{a}_{\alpha}\times\boldsymbol{R}^{\alpha} + \frac{p\tilde{H}}{\sqrt{A}}\boldsymbol{a}_3\times(\boldsymbol{a}_1\times\boldsymbol{a}_2) = \frac{\rho\tilde{\tau}H^2}{2}\boldsymbol{a}_3\times\ddot{\boldsymbol{a}}_3 \tag{24b}$$

The first equation corresponds to the linear momentum balance and the second to the angular momentum balance.

- **The boundary conditions** are

- force boundary conditions: $\forall t, \forall \mathbf{P}_0 \in \partial S_0$,

$$\boldsymbol{R}^{\alpha}\nu_{0\alpha} - p\tilde{H}\mathbf{P}_{,s_0}\times\boldsymbol{a}_3 = \boldsymbol{q}' \tag{25}$$

- moment boundary conditions: $\forall t$, $\forall \mathbf{P}_0 \in \partial S_0$,

$$\boldsymbol{L}^{\beta}\nu_{0\beta}\cdot\boldsymbol{a}^{\alpha}\nu_{0\alpha} - \frac{p\tilde{H}^3}{12}(\boldsymbol{a}_{3,s_0}\times\boldsymbol{a}_3)\cdot\boldsymbol{a}^{\alpha}\nu_{0\alpha} = \|\boldsymbol{a}^3\|\Gamma^s\boldsymbol{\nu}\cdot\boldsymbol{a}^{\alpha}\nu_{0\alpha} \tag{26a}$$

$$\boldsymbol{L}^{\beta}\nu_{0\beta}\cdot\boldsymbol{a}^{\alpha}s_{0\alpha} - \frac{p\tilde{H}^3}{12}(\boldsymbol{a}_{3,s_0}\times\boldsymbol{a}_3)\cdot\boldsymbol{a}^{\alpha}s_{0\alpha} = \|\boldsymbol{a}^3\|\left(\Gamma^s\boldsymbol{\nu}\cdot\boldsymbol{a}^{\alpha}s_{0\alpha} - \Gamma^{\nu}\boldsymbol{s}\cdot\boldsymbol{a}^{\alpha}s_{0\alpha}\right) \tag{26b}$$

Proof. Since the principle of virtual power (7) holds for arbitrary $\boldsymbol{U}^*$ and $\boldsymbol{\omega}^*$, it leads to Eq. (24a) and the following equation: $\forall t$, $\forall \mathbf{P}_0 \in S_0$,

$$\boldsymbol{a}_3\times\frac{1}{\sqrt{A}}\left(\sqrt{A}\boldsymbol{L}^{\alpha}\right)_{,\alpha} - \boldsymbol{a}_3\times\boldsymbol{S} + \frac{p\tilde{H}}{\sqrt{A}}\boldsymbol{a}_3\times(\boldsymbol{a}_1\times\boldsymbol{a}_2) = \frac{\rho\tilde{\tau}H^2}{2}\boldsymbol{a}_3\times\ddot{\boldsymbol{a}}_3$$

By calculating $\boldsymbol{a}_{\alpha}\times\boldsymbol{R}^{\alpha}$, $\boldsymbol{a}_{3,\alpha}\times\boldsymbol{L}^{\alpha}$ and $\boldsymbol{a}_3\times\boldsymbol{S}$ from expressions (13), one can easily verify that the following equality holds:

$$\boldsymbol{a}_{\alpha}\times\boldsymbol{R}^{\alpha} + \boldsymbol{a}_{3,\alpha}\times\boldsymbol{L}^{\alpha} + \boldsymbol{a}_3\times\boldsymbol{S} = \mathbf{0}$$

Furthermore, it can also be shown that

$$\boldsymbol{a}_3 \times \frac{1}{\sqrt{A}}\big(\sqrt{A}\boldsymbol{L}^\alpha\big)_{,\alpha} = \frac{1}{\sqrt{A}}\big(\sqrt{A}\boldsymbol{a}_3 \times \boldsymbol{L}^\alpha\big)_{,\alpha} - \boldsymbol{a}_{3,\alpha} \times \boldsymbol{L}^\alpha$$

Combining the two previous equations yields Eq. (24b). The principle of virtual power (7) also yields the two following boundary conditions written on edge ∂S_0: the first one is Eq. (25) and the second is

$$\forall t, \forall \mathbf{P}_0 \in \partial S_0, \quad \boldsymbol{a}_3 \times \boldsymbol{L}^\alpha \nu_{0\alpha} - \frac{p\tilde{H}^3}{12}\boldsymbol{a}_{3,s_0} - \boldsymbol{\Gamma} = \boldsymbol{0} \tag{27}$$

On account of the following properties:

$$\forall \boldsymbol{v} \in \mathbb{R}^3,\ \boldsymbol{a}_3 \times \boldsymbol{v} = \boldsymbol{0} \quad \Leftrightarrow \quad \forall \alpha \in \{1,2\},\ \boldsymbol{v} \cdot \boldsymbol{a}^\alpha = 0 \quad \Leftrightarrow \quad \begin{cases} \boldsymbol{v} \cdot \boldsymbol{a}^\alpha \nu_{0\alpha} = 0 \\ \boldsymbol{v} \cdot \boldsymbol{a}^\alpha s_{0\alpha} = 0 \end{cases} \tag{28}$$

Relation (27) then gives (26). ■

4. Linearized equations

The equations of motion (24)–(26), where the internal forces $\boldsymbol{R}^\alpha$ and $\boldsymbol{L}^\alpha$ are functions of the stress resultants $N^{\alpha\beta}$, $M^{\alpha\beta}$, $M^{(2)\alpha\beta}$, Q^β and $Q^{(1)\beta}$ via Relations (12) and (13), are nonlinear equations in terms of the displacements $\boldsymbol{U}$ and $\boldsymbol{a}_3$. In the sequel, we assume that the inflatable panel undergoes small displacements and rotations and we shall derive the linearized equations from the above-found nonlinear equations.

It should be emphasized that one has to formulate the problem in the nonlinear framework as done in the previous sections, before proceeding to the linearization. On the contrary, if the equations were obtained directly from the linear context assuming small strains, the essential terms pertaining to the inflation pressure, which is a follower load, would be missing.

4.1. Small displacements and rotations

The linearization will be carried out around the *pre-stressed reference configuration*, under the following assumptions:

i) The mid-surface displacements $\boldsymbol{U} \equiv \boldsymbol{x} - \boldsymbol{X}$ and its derivatives with respect to the spatial coordinates and time t are assumed to be infinitesimal of the *first order*.

ii) The fiber rotation vector $\boldsymbol{\psi} \equiv \boldsymbol{a}_3 - \boldsymbol{e}_3$ is assumed to be infinitesimal of the *first order*. Its derivatives with respect to the spatial coordinates and time t are also small of the first order.

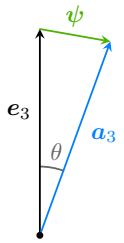

Figure 8: The fiber rotates by a small angle θ in the deformed configuration.

The linearized equations will be obtained by discarding infinitesimals of the second order and higher. Let the angle between the unit vectors $\boldsymbol{e}_3$ and $\boldsymbol{a}_3$ be θ, Fig. 8. Since $\|\boldsymbol{\psi}\| = 2\sin\frac{\theta}{2}$, assuming that $\boldsymbol{\psi}$ is small of the first order amounts to assuming that angle θ is small. Moreover, since $\boldsymbol{\psi}\cdot\boldsymbol{e}_3 = 1-\cos\theta = 2\sin^2\frac{\theta}{2}$, the out-of-plane component ψ_3 of $\boldsymbol{\psi}$ is of second order and can be neglected.

4.2. Basis vectors

Calculations can be made simpler by temporarily setting the curvilinear coordinates (ξ^1, ξ^2) to be equal to the Cartesian coordinates (X, Y), meaning that $(\boldsymbol{A}_1, \boldsymbol{A}_2, \boldsymbol{e}_3) = (\boldsymbol{e}_1, \boldsymbol{e}_2, \boldsymbol{e}_3)$. Once the linearization is achieved, we will go back to component-free notations, which are independent of any particular coordinate system. The components of $\boldsymbol{U}$ are

$$\boldsymbol{U} = \boldsymbol{U}^P + W\boldsymbol{e}_3 = U_1\boldsymbol{e}_1 + U_2\boldsymbol{e}_2 + W\boldsymbol{e}_3$$

where the notation $\bullet^P$ is used to indicate in-plane quantities and $\boldsymbol{U}^P = U_\alpha\boldsymbol{e}_\alpha$ is the projection of $\boldsymbol{U}$ in the plane $\boldsymbol{e}_1\boldsymbol{e}_2$. Thus, the natural covariant basis vectors in Eq. (3) can be written as

$$\boldsymbol{a}_\alpha = \boldsymbol{e}_\alpha + \boldsymbol{U}^P_{,\alpha} + W_{,\alpha}\boldsymbol{e}_3$$

4.3. Strain tensor

The Green strain components in Relation (6) can be rewritten in terms of $\boldsymbol{U}^P$ and $\boldsymbol{\psi}$. Discarding terms of order 2 and above leads to

$$\begin{aligned}
\boldsymbol{E}^{(0)} &= \frac{1}{2}\left(\mathbf{grad}\,\boldsymbol{U}^P + \mathbf{grad}^{\mathsf{T}}\,\boldsymbol{U}^P\right) &&= \textsc{sym}\,\mathbf{grad}\boldsymbol{U}^P \\
\boldsymbol{E}^{(1)} &= \frac{1}{2}\left(\mathbf{grad}\,\boldsymbol{\psi} + \mathbf{grad}^{\mathsf{T}}\,\boldsymbol{\psi}\right) &&= \textsc{sym}\,\mathbf{grad}\boldsymbol{\psi} \\
\boldsymbol{E}^{(2)} &= \mathbf{0} \\
E_{\alpha 3} &= \frac{1}{2}(\psi_\alpha + W_{,\alpha})
\end{aligned} \tag{29}$$

where the symbol **sym** designates the symmetric part of a tensor.

4.4. Stress resultants and internal forces

The response of the membrane material is assumed to be isotropic and based on a hyperelastic model. There exists a great variety of hyperelastic constitutive laws that take different forms and involve different material parameters. Fortunately enough, the common feature of the hyperelastic laws is that all of them reduce to the standard linear Saint Venant-Kirchhoff law within the context of small deformations. As a result, one has only to consider the Saint Venant-Kirchhoff law when carrying out the linearization of the governing equations:

$$\boldsymbol{\Sigma} = \boldsymbol{\Sigma}_0 + 2\mu\boldsymbol{E} + \lambda(\mathrm{tr}\,\boldsymbol{E})\boldsymbol{I} \tag{30}$$

where $\boldsymbol{\Sigma}_0$ is the pre-stress tensor and λ, μ are the Lamé parameters. Furthermore, the membranes are assumed to be under plane stress in the current configuration, which means that, at any point in domain Ω,

$$\sigma^{13} = \sigma^{23} = \sigma^{33} = 0 \quad \Leftrightarrow \quad \Sigma^{13} = \Sigma^{23} = \Sigma^{33} = 0$$

The same assumption is made on the reference stress state: $\Sigma_0^{13} = \Sigma_0^{23} = \Sigma_0^{33} = 0$. The zero normal stress hypothesis $\Sigma^{33} = 0$ (or, equivalently, $\sigma^{33} = 0$) leads to the so-called *reduced constitutive law*:

$$\forall \alpha, \beta \in \{1, 2\}, \quad \Sigma^{\alpha\beta} = \Sigma_0^{\alpha\beta} + K^{\alpha\beta\delta\gamma} E_{\delta\gamma} \tag{31}$$

where

$$K^{\alpha\beta\delta\gamma} = \frac{E}{1-\nu^2}\left(\frac{1}{2}(1-\nu)\left(A^{\alpha\gamma}A^{\beta\delta} + A^{\alpha\delta}A^{\beta\gamma}\right) + \nu A^{\alpha\beta}A^{\gamma\delta}\right)$$

and E is the Young modulus, ν the Poisson's ratio. The pre-stress resultants induced by the internal pressure are calculated from Relation (12): $\forall \alpha, \beta \in \{1,2\}$,

$$\begin{aligned} N_0^{\alpha\beta} &= \int_T \Sigma_0^{\alpha\beta}\,\mathrm{d}Z &&= 2\tau\Sigma_0^{\alpha\beta} \\ M_0^{\alpha\beta} &= \int_T Z\Sigma_0^{\alpha\beta}\,\mathrm{d}Z &&= 0 \\ M_0^{(2)\alpha\beta} &= \int_T Z^2\Sigma_0^{\alpha\beta}\,\mathrm{d}Z &&= \frac{\tilde{\tau}H^2}{2}\Sigma_0^{\alpha\beta} \end{aligned} \tag{32}$$

The stress resultants defined in Relation (12) are evaluated by performing the integrations over interval T. Taking into account the reduced constitutive law (31) and Relation (29) gives the resultants written in component-free notations:

$$\begin{aligned} \boldsymbol{N} &= \boldsymbol{N}_0 + \frac{2E\tau}{1-\nu^2}\left((1-\nu)\mathbf{sym}\,\mathbf{grad}\boldsymbol{U}^P + \nu\big(\operatorname{div}\boldsymbol{U}^P\big)\boldsymbol{I}^P\right) \\ \boldsymbol{M} &= \frac{E\tilde{\tau}H^2}{2(1-\nu^2)}\left((1-\nu)\mathbf{sym}\,\mathbf{grad}\boldsymbol{\psi} + \nu\big(\operatorname{div}\boldsymbol{\psi}\big)\boldsymbol{I}^P\right) \\ \boldsymbol{M}^{(2)} &= \boldsymbol{M}_0^{(2)} + \frac{E\tilde{\tau}H^2}{2(1-\nu^2)}\left((1-\nu)\mathbf{sym}\,\mathbf{grad}\boldsymbol{U}^P + \nu\big(\operatorname{div}\boldsymbol{U}^P\big)\boldsymbol{I}^P\right) \\ \boldsymbol{Q} &= \boldsymbol{0} \\ \boldsymbol{Q}^{(1)} &= \boldsymbol{0} \end{aligned} \tag{33}$$

where $\boldsymbol{I}^P = \boldsymbol{e}_\alpha \otimes \boldsymbol{e}_\alpha$ is the identity tensor restricted to the plane $\boldsymbol{e}_1\boldsymbol{e}_2$. These relations are used to compute stresses after having found a solution to the problem. Substituting the linearized expressions of the stress resultants of Eq. (33) into Eq. (13) leads to

$$\boldsymbol{R}^\beta = N_0^{\alpha\beta}(\boldsymbol{e}_\alpha + \boldsymbol{U}_{,\alpha}) + \frac{2E\tau}{1-\nu^2}\left(\frac{1-\nu}{2}(U_{\beta,\alpha} + U_{\alpha,\beta}) + \nu\delta^{\alpha\beta}U_{\gamma,\gamma}\right)\boldsymbol{e}_\alpha \tag{34}$$

$$\boldsymbol{L}^\beta = \frac{E\tilde{\tau}H^2}{2(1-\nu^2)}\left(\frac{1-\nu}{2}(\psi_{\alpha,\beta} + \psi_{\beta,\alpha}) + \nu\delta^{\alpha\beta}\psi_{\gamma,\gamma}\right)\boldsymbol{e}_\alpha + M_0^{(2)\alpha\beta}\boldsymbol{\psi}_{,\alpha} \tag{35}$$

Note that the pre-stress bending moment of order two, $M_0^{(2)\alpha\beta}$, in the last equation has

been obtained thanks to the correct linearization process described at the beginning of this section. It would not have been found if we had considered the linear framework from the start. It is analogous to the term pI_0/S_0 in previous works on inflatable beams [9].

4.5. External loads other than the internal pressure

The expressions of the external loads in Eq. (26) must also be linearized. After linearization, one gets $\|\boldsymbol{a}^3\| = 1$. The linearized expressions of the dual basis vectors $\boldsymbol{a}^i$ leads to

$$\begin{aligned}
\boldsymbol{\nu} \cdot \boldsymbol{a}^\alpha \nu_{0\alpha} &= 1 - \boldsymbol{\nu}_0 \cdot \mathbf{grad}\, \boldsymbol{U}^P \cdot \boldsymbol{\nu}_0 \\
\boldsymbol{\nu} \cdot \boldsymbol{a}^\alpha s_{0\alpha} &= -2\boldsymbol{s}_0 \cdot \mathbf{sym}\, \mathbf{grad} \boldsymbol{U}^P \cdot \boldsymbol{\nu}_0 \\
\boldsymbol{s} \cdot \boldsymbol{a}^\alpha s_{0\alpha} &= 1 - \boldsymbol{s}_0 \cdot \mathbf{grad}\, \boldsymbol{U}^P \cdot \boldsymbol{s}_0
\end{aligned}$$

The right-hand sides of Eq. (26) then become

$$\|\boldsymbol{a}^3\| \Gamma^s \boldsymbol{\nu} \cdot \boldsymbol{a}^\alpha \nu_{0\alpha} = \big(1 - \boldsymbol{\nu}_0 \cdot \mathbf{grad}\, \boldsymbol{U}^P \cdot \boldsymbol{\nu}_0\big)\Gamma^s$$

$$\|\boldsymbol{a}^3\| \big(\Gamma^s \boldsymbol{\nu} \cdot \boldsymbol{a}^\alpha s_{0\alpha} - \Gamma^\nu \boldsymbol{s} \cdot \boldsymbol{a}^\alpha s_{0\alpha}\big) = -\big(2\boldsymbol{s}_0 \cdot \mathbf{sym}\, \mathbf{grad} \boldsymbol{U}^P \cdot \boldsymbol{\nu}_0\big)\Gamma^s - \big(1 - \boldsymbol{s}_0 \cdot \mathbf{grad}\, \boldsymbol{U}^P \cdot \boldsymbol{s}_0\big)\Gamma^\nu$$

4.6. Internal pressure load

Taking into account the expressions of $\boldsymbol{a}_\alpha$ and $\boldsymbol{a}_3$, the pressure term in equation of motion (24a) becomes

$$\frac{p\tilde{H}}{\sqrt{A}}\big(\boldsymbol{a}_{3,1} \times \boldsymbol{a}_2 + \boldsymbol{a}_1 \times \boldsymbol{a}_{3,2}\big) = \frac{p\tilde{H}}{\sqrt{A}}\big(\boldsymbol{\psi}_{,1} \times \boldsymbol{e}_2 + \boldsymbol{e}_1 \times \boldsymbol{\psi}_{,2}\big) \tag{36}$$

Note that $\sqrt{A} = 1$ because the basis is orthonormal. First, projecting Relation (36) on $\boldsymbol{a}^\alpha$ yields

$$\forall \alpha \in \{1, 2\}, \quad (\boldsymbol{\psi}_{,1} \times \boldsymbol{e}_2 + \boldsymbol{e}_1 \times \boldsymbol{\psi}_{,2}) \cdot \boldsymbol{a}^\alpha = \boldsymbol{\psi}_{,1} \cdot (\boldsymbol{e}_2 \times \boldsymbol{e}_\alpha) + (\boldsymbol{e}_\alpha \times \boldsymbol{e}_1) \cdot \boldsymbol{\psi}_{,2} = 0$$

since $\boldsymbol{\psi}$ and its derivatives are perpendicular to $\boldsymbol{e}_3$. Then, projecting Eq. (36) on $\boldsymbol{a}^3$ yields

$$\begin{aligned}
(\boldsymbol{\psi}_{,1} \times \boldsymbol{e}_2 + \boldsymbol{e}_1 \times \boldsymbol{\psi}_{,2}) \cdot \boldsymbol{a}^3 &= \boldsymbol{\psi}_{,1} \cdot (\boldsymbol{e}_2 \times \boldsymbol{e}_3) + (\boldsymbol{e}_3 \times \boldsymbol{e}_1) \cdot \boldsymbol{\psi}_{,2} \\
&= \boldsymbol{\psi}_{,1} \cdot \boldsymbol{e}_1 + \boldsymbol{\psi}_{,2} \cdot \boldsymbol{e}_2 = \psi_{1,1} + \psi_{2,2} = \operatorname{div} \boldsymbol{\psi}
\end{aligned}$$

The pressure term in equation of motion (24b) becomes

$$\boldsymbol{a}_3 \times \big(\boldsymbol{a}_1 \times \boldsymbol{a}_2\big) = \boldsymbol{a}_3 \times \big((\boldsymbol{e}_1 + \boldsymbol{U}_{,1}) \times (\boldsymbol{e}_2 + \boldsymbol{U}_{,2})\big)$$

The second order terms are neglected, leaving only

$$\begin{aligned}\boldsymbol{a}_3 \times \big(\boldsymbol{a}_1 \times \boldsymbol{a}_2\big) &\approx \boldsymbol{\psi} \times \big(\boldsymbol{e}_1 \times \boldsymbol{e}_2\big) + W_{,2}\boldsymbol{e}_1 - W_{,1}\boldsymbol{e}_2 \\ &= \big(\boldsymbol{\psi} + W_{,1}\boldsymbol{e}_1 + W_{,2}\boldsymbol{e}_2\big) \times \boldsymbol{e}_3 = (\boldsymbol{\psi} + \mathbf{grad}\, W) \times \boldsymbol{e}_3\end{aligned}$$

Likewise, the pressure line force on the edge in boundary condition (25) writes

$$p\tilde{H}\mathbf{P}_{,s_0} \times \boldsymbol{a}_3 \approx p\tilde{H}\big(\mathbf{P}_{0,s_0} \times \boldsymbol{\psi} + \boldsymbol{U}_{,s_0} \times \boldsymbol{e}_3\big)$$

The last term to be linearized is the pressure term in boundary conditions (26):

$$\begin{aligned}\frac{p\tilde{H}^3}{12}(\boldsymbol{a}_{3,s_0} \times \boldsymbol{a}_3) \cdot \boldsymbol{a}^\alpha \nu_{0\alpha} &\approx \frac{p\tilde{H}^3}{12}\boldsymbol{\psi}_{,s_0} \cdot \boldsymbol{s}_0 \\ \frac{p\tilde{H}^3}{12}(\boldsymbol{a}_{3,s_0} \times \boldsymbol{a}_3) \cdot \boldsymbol{a}^\alpha s_{0\alpha} &\approx -\frac{p\tilde{H}^3}{12}\boldsymbol{\psi}_{,s_0} \cdot \boldsymbol{\nu}_0\end{aligned}$$

4.7. Inertial quantities

The only fact worth noting for the inertial quantities is that the inertial term in the moment equation (24b) should be linearized as follows:

$$\frac{\rho\tilde{\tau}H^2}{2}\boldsymbol{a}_3 \times \ddot{\boldsymbol{a}}_3 = \frac{\rho\tilde{\tau}H^2}{2}\boldsymbol{a}_3 \times \ddot{\boldsymbol{\psi}}$$

It is more convenient to keep $\boldsymbol{a}_3$ as is in the last right-hand side and not to replace it with $\boldsymbol{\psi} + \boldsymbol{e}_3$, since this enables one to more easily obtain the final expression of the moment equation (39) below.

4.8. Linearized governing equations

We eventually arrive to the desired linearized equations by using the above ingredients. The results are written below in component-free notations which are independent of the coordinate system.

• **The linearized equations of motion** are

- the linear momentum balance of in-plane forces: $\forall t$, $\forall \mathbf{P}_0 \in S_0$,

$$\boldsymbol{N}_0 : \mathbf{grad}\,\mathbf{grad}\,\boldsymbol{U}^P + \frac{E\tau}{1-\nu^2}\Big[(1-\nu)\boldsymbol{\Delta}\boldsymbol{U}^P + (1+\nu)\,\mathbf{grad}\,\mathrm{div}\,\boldsymbol{U}^P\Big] + \boldsymbol{q}\cdot\boldsymbol{a}^\alpha = 2\tau\rho\ddot{\boldsymbol{U}}^P \quad (37)$$

- the linear momentum balance of out-of-plane forces: $\forall t$, $\forall \mathbf{P}_0 \in S_0$,

$$\boldsymbol{N}_0 : \mathbf{grad}\,\mathbf{grad}\,W + p\tilde{H}\,\mathrm{div}\,\boldsymbol{\psi} + \boldsymbol{q}\cdot\boldsymbol{a}^3 = 2\tau\rho\ddot{W} \quad (38)$$

- the angular momentum balance: $\forall t$, $\forall \mathbf{P}_0 \in S_0$,

$$\begin{aligned}&\frac{E\tilde{\tau}H^2}{4(1-\nu^2)}\Big[(1-\nu)\boldsymbol{\Delta}\boldsymbol{\psi} + (1+\nu)\,\mathbf{grad}\,\mathrm{div}\,\boldsymbol{\psi}\Big] + \mathbf{div}\left(\mathbf{grad}\,\boldsymbol{\psi}\cdot\boldsymbol{M}_0^{(2)}\right)\\ &- p\tilde{H}\,(\boldsymbol{\psi} + \mathbf{grad}\,W) = \frac{\rho\tilde{\tau}H^2}{2}\ddot{\boldsymbol{\psi}}\end{aligned} \quad (39)$$

• The two **force boundary conditions** are

- for in-plane forces: $\forall t$, $\forall \mathbf{P}_0 \in \partial S_0$,

$$\begin{aligned}&\frac{2E\tau}{1-\nu^2}\left((1-\nu)\,\mathbf{sym}\,\mathbf{grad}\boldsymbol{U}^P + \nu\big(\mathrm{div}\,\boldsymbol{U}^P\big)\boldsymbol{I}\right)\cdot\boldsymbol{\nu}_0\\ &+ p\tilde{H}\big[\,\mathbf{grad}\,\boldsymbol{U}^P\cdot\boldsymbol{\nu}_0 + \boldsymbol{U}^P_{,s_0}\times\boldsymbol{e}_3\big] = \boldsymbol{q}'\cdot\boldsymbol{a}^\alpha\end{aligned} \quad (40)$$

- for out-of-plane forces: $\forall t$, $\forall \mathbf{P}_0 \in \partial S_0$,

$$p\tilde{H}\big(\boldsymbol{\psi} + \mathbf{grad}\,W\big)\cdot\boldsymbol{\nu}_0 = \boldsymbol{q}\cdot\boldsymbol{a}^3 \quad (41)$$

• The two **moment boundary conditions** are

- moments normal to the border: $\forall t$, $\forall \mathbf{P}_0 \in \partial S_0$,

$$\begin{aligned}&\frac{E\tilde{\tau}H^2}{2(1-\nu^2)}\Big[(1-\nu)\boldsymbol{\nu}_0\cdot\,\mathbf{sym}\,\mathbf{grad}\boldsymbol{\psi}\cdot\boldsymbol{\nu}_0 + \nu\,\mathrm{div}\,\boldsymbol{\psi}\Big] + \boldsymbol{\nu}_0\cdot\mathbf{grad}\,\boldsymbol{\psi}\cdot\boldsymbol{M}_0^{(2)}\cdot\boldsymbol{\nu}_0 + \frac{p\tilde{H}^3}{12}\boldsymbol{\psi}_{,s_0}\cdot\boldsymbol{s}_0\\ &= \big(1-\boldsymbol{\nu}_0\cdot\mathbf{grad}\,\boldsymbol{U}^P\cdot\boldsymbol{\nu}_0\big)\,\Gamma^s\end{aligned} \quad (42)$$

- moments tangent to the border: $\forall t$, $\forall \mathbf{P}_0 \in \partial S_0$,

$$\begin{aligned} &\frac{E\tilde{\tau}H^2}{2(1-\nu^2)}(1-\nu)\boldsymbol{s}_0 \cdot \textsc{sym}\,\mathbf{grad}\boldsymbol{\psi} \cdot \boldsymbol{\nu}_0 + \boldsymbol{s}_0 \cdot \mathbf{grad}\,\boldsymbol{\psi} \cdot \boldsymbol{M}_0^{(2)} \cdot \boldsymbol{\nu}_0 - \frac{p\tilde{H}^3}{12}\boldsymbol{\psi}_{,s_0} \cdot \boldsymbol{\nu}_0 \\ &= -\left(2\boldsymbol{s}_0 \cdot \textsc{sym}\,\mathbf{grad}\boldsymbol{U}^P \cdot \boldsymbol{\nu}_0\right)\Gamma^s - \left(1 - \boldsymbol{s}_0 \cdot \mathbf{grad}\,\boldsymbol{U}^P \cdot \boldsymbol{s}_0\right)\Gamma^\nu \end{aligned} \tag{43}$$

Proof. The linear momentum equations (37) and (38) are obtained by substituting $\boldsymbol{R}^\alpha_{,\alpha}$ from Eq. (34) into Eq. (24a). The equivalence (28) is applied to Eq. (24b) with the expression of $\boldsymbol{L}^\beta$ in Eq. (35) to produce the angular momentum equations (39). As for the boundary conditions, substituting Eq. (34) into Eq. (25) yields (40) and (41). Likewise, using Eq. (35) to rewrite Eq. (26) yields (42) and (43). ■

All the governing equations contain at least one term that corresponds to the effect of the internal pressure on the panel, either via p or the pre-tension $\boldsymbol{N}_0$ or the pre-moment of second order $\boldsymbol{M}_0^{(2)}$.

5. Analytical solution for a circular inflatable panel

Let us show how to solve the foregoing linearized equations for the static bending of a simply-supported circular inflatable panel subjected to a uniform vertical load. This problem admits an analytical solution as the geometry, the loading and the boundary conditions are simple.

5.1. Determination of the reference configuration

In the previous sections, the theory was built assuming that the reference configuration was known. In practice however, one only knows the natural configuration – where there is no external loading and the stress state is zero throughout the body – and one thus has to determine the pre-stressed reference configuration thereafter.

In the natural state, the geometry of the panel is described by the natural radius $R_\varnothing$ and the natural height $H_\varnothing$. On the other hand, after inflation, the panel's reference geometry is described by radius R and height H. Obtaining (R, H) from $(R_\varnothing, H_\varnothing)$, for each inflation pressure p, is a preliminary linear elastic calculation which should be carried out beforehand.

The reference height of the panel can be satisfactorily estimated by assuming that the increase in total height is entirely due to the elongation of the drop-stitch yarns (discarding the bulge on the edge of the panel). Given the Young modulus E_y, the section area S_y of a single drop-stitch yarn and the drop yarns density d (number of yarns per square meter), the formula is simply:

$$H \approx H_\varnothing \left(1 + \frac{p}{E_y S_y d}\right) \tag{44}$$

For numerical purposes, the product $E_y S_y$ is set to 100 N and d to 30,000 m^{-2}. Again, a simple calculation discarding the lateral bulge yields the reference radius with high accuracy:

$$R \approx R_\varnothing \left(1 + \frac{p\tilde{H}}{2\tau}\frac{1-\nu}{E}\right) \tag{45}$$

The natural dimensions $R_\varnothing$, $H_\varnothing$, τ and the material properties are given in Table 1. For each stress-free geometry, four inflation pressures p are considered (30 kPa, 50 kPa, 70 kPa and 90 kPa) which give rise to four different reference geometries each described by R and H. All the numerical values are chosen in accordance with typical values for coated fabrics [1]. The numerical values for R and H in Table 2 are computed from Relations (44) and (45).

Parameter	Values
$R_\varnothing$	1.5 m
$H_\varnothing$	10 cm, 20 cm
τ	0.66 mm
E	2.5 GPa
ν	0.25

Table 1: Geometry in the natural state and material properties of the inflatable panel.

5.2. Analytical solution

Let $\boldsymbol{q} = q\boldsymbol{e}_3$ denote the uniform, vertical dead load applied over the mid-surface S_0 and (r, θ, z) the cylindrical coordinates of any point of the panel (Fig. 9). Since the static bending problem is axisymmetric around the axis $(\mathbf{O}; \boldsymbol{e}_3)$, the unknown fields W and $\boldsymbol{\psi}$ are functions of the radial distance r only. The inflation pressure p induces an isotropic plane

$R_\varnothing$ (m)	$H_\varnothing$ (cm)	p (kPa)	R (m)	H (cm)
1.5	10	30	1.501	10.10
		50	1.502	10.17
		70	1.502	10.23
		90	1.503	10.30
	20	30	1.502	20.20
		50	1.503	20.33
		70	1.504	20.47
		90	1.506	20.60

Table 2: Analytically determined radii and heights of the inflated panel before and after inflation.

pre-stress in the membranes, which is expressed in the cylindrical basis $(\boldsymbol{e}_r, \boldsymbol{e}_\theta, \boldsymbol{e}_3)$ as

$$\mathrm{Mat}(\boldsymbol{\Sigma}_0; \boldsymbol{e}_r\boldsymbol{e}_\theta\boldsymbol{e}_3) = \frac{p\tilde{H}}{2\tau}\begin{bmatrix} 1 & 0 & 0 \\ 0 & 1 & 0 \\ 0 & 0 & 0 \end{bmatrix}$$

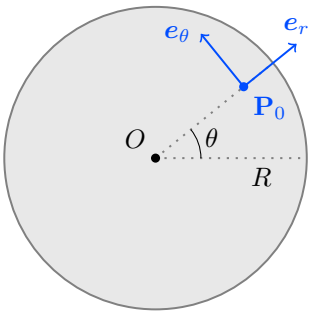

Figure 9: Geometry of the circular panel and local basis.

Hence, the matrices of pre-tension $\boldsymbol{N}_0$ and pre-moment $\boldsymbol{M}_0^{(2)}$ after integrating through the thickness are

$$\mathrm{Mat}(\boldsymbol{N}_0; \boldsymbol{e}_r\boldsymbol{e}_\theta\boldsymbol{e}_3) = p\tilde{H}\begin{bmatrix} 1 & 0 & 0 \\ 0 & 1 & 0 \\ 0 & 0 & 0 \end{bmatrix}$$

$$\mathrm{Mat}(\boldsymbol{M}_0^{(2)};\boldsymbol{e}_r\boldsymbol{e}_\theta\boldsymbol{e}_3)=\frac{pH^2\tilde{H}\tilde{\tau}}{4\tau}\begin{bmatrix}1&0&0\\0&1&0\\0&0&0\end{bmatrix}$$

After discarding time-dependent terms, Eq. (38) and (39) become, in polar coordinates:

$$\frac{1}{r}\big(r(W_{,r}+\psi_r)\big)_{,r}=-\frac{q}{p\tilde{H}} \tag{46}$$

$$-K\left(\psi_{r,rr}+\frac{\psi_{r,r}}{r}-\frac{\psi_r}{r^2}\right)+p\tilde{H}(W_{,r}+\psi_r)=0 \tag{47}$$

where $K=\dfrac{E\tilde{\tau}H^2}{2(1-\nu^2)}+\dfrac{pH^2\tilde{H}\tilde{\tau}}{4\tau}>0$. The boundary condition are $W(R)=0$ and Eq. (42) with $\Gamma^s=\Gamma^\theta=0$:

$$K\psi_{r,r}(R)+K'\frac{\psi_r(R)}{R}=0 \tag{48}$$

where $K'=\dfrac{\nu E\tilde{\tau}H^2}{2(1-\nu^2)}+\dfrac{p\tilde{H}^3}{12}>0$. Integrating Relation (46) with respect to r gives

$$W_{,r}+\psi_r=-\frac{q}{p\tilde{H}}\left(\frac{r}{2}+\frac{C_1}{r}\right) \tag{49}$$

where C_1 is a constant of integration. Using Relation (47), one obtains a differential equation of unknown ψ_r, which is a Cauchy-Euler equation:

$$r^2\psi_{r,rr}+r\psi_{r,r}-\psi_r=-\frac{q}{K}\left(\frac{r^3}{2}+C_1r\right) \tag{50}$$

With the change of variables $r=\exp x \Leftrightarrow x=\log r$ (with $r>0$) and $z(x)=\psi_r(r)=\psi_r(\exp x)$, the associated homogeneous equation is

$$\frac{\mathrm{d}^2z}{\mathrm{d}x^2}-z=0$$

The solution is $z(x)=C_2\exp(x)+C_3\exp(-x)$ where C_2 and C_3 are constants of integration. Hence the solution to the homogeneous equation corresponding to Eq. (50):

$$\psi_r(r)=C_2r+\frac{C_3}{r}$$

The method of variation of parameters is used to find the solution to Eq. (50). The following system of equations is obtained:

$$\begin{cases} r^2 C_2' + C_3' = 0 \\ r^2 C_2' - C_3' = -\dfrac{q}{K}\left(\dfrac{r^3}{2} + C_1 r\right) \end{cases} \Rightarrow \begin{cases} C_2 = -\dfrac{q}{2K}\left(\dfrac{r^2}{4} + C_1 \log r\right) + C_4 \\ C_3 = \quad \dfrac{q}{2K}\left(\dfrac{r^4}{8} + C_1 \dfrac{r^2}{2}\right) + C_5 \end{cases}$$

where C_4 and C_5 are new constants of integration. Substituting C_2 and C_3 in the expression of ψ_r writes

$$\psi_r = \frac{q}{2K}\left(-\frac{r^3}{8} + C_1\frac{r}{2} - C_1 r \log r\right) + C_4 r + \frac{C_5}{r}$$

Given that the problem is axisymmetric, one must have $\lim_{r\to 0} \psi_r(r) = 0$, which implies $C_5 = 0$. The deflection W can then be derived from Relation (49):

$$W_{,r} = -\frac{q}{2K}\left(-\frac{r^3}{8} + C_1\frac{r}{2} - C_1 r \log r\right) - C_4 r - \frac{q}{p\tilde{H}}\left(\frac{r}{2} + \frac{C_1}{r}\right)$$

The constants of integration are deduced from the boundary conditions and physical considerations. It follows that:

$$\begin{cases} W(r) = q(R^2 - r^2)\left(\dfrac{1}{4p\tilde{H}} + \dfrac{1}{64K}\left(\dfrac{5K + K'}{K + K'}R^2 - r^2\right)\right) \\ \psi_r(r) = \dfrac{q}{16K} r\left(\dfrac{3K + K'}{K + K'}R^2 - r^2\right) \end{cases} \tag{51}$$

While the deflection W and the fiber rotation $\boldsymbol{\psi}$ depend linearly on the load q, they are intricate functions of pressure p via the ratio $1/4p\tilde{H}$ and the coefficients K and K'.

Let us now plot the solution (51) using the geometric quantities $R_\varnothing$ and $H_\varnothing$ in the natural state, τ and the material properties E and ν from Table 1 and taking the external surface load $q = 100$ Pa. Fig. 10 shows the plots of the deflection W and the fiber rotation ψ_r for four different inflation pressures p and two panel heights $H_\varnothing$. As expected, the deflection becomes lower as the pressure p increases, which reflects the stiffening phenomenon of inflatable panels, i.e. the increase in bending stiffness with pressurization. Also, the deflection decreases when the height H increases since the pre-stress $\boldsymbol{N}_0$ is proportional to $\tilde{H}$, creating additional structural stiffness. As regards the change of the fiber rotation ψ_r, it

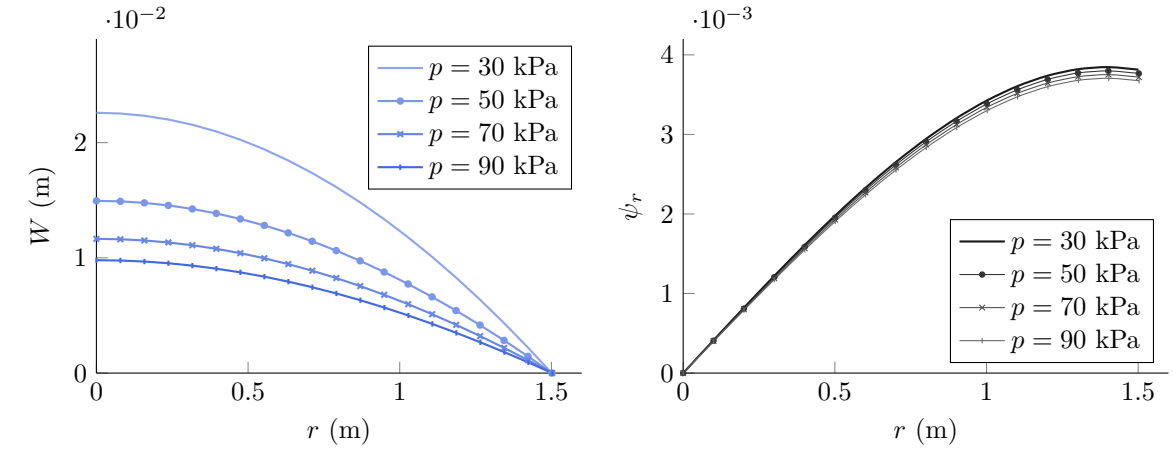

(a) $H_\varnothing = 10$ cm

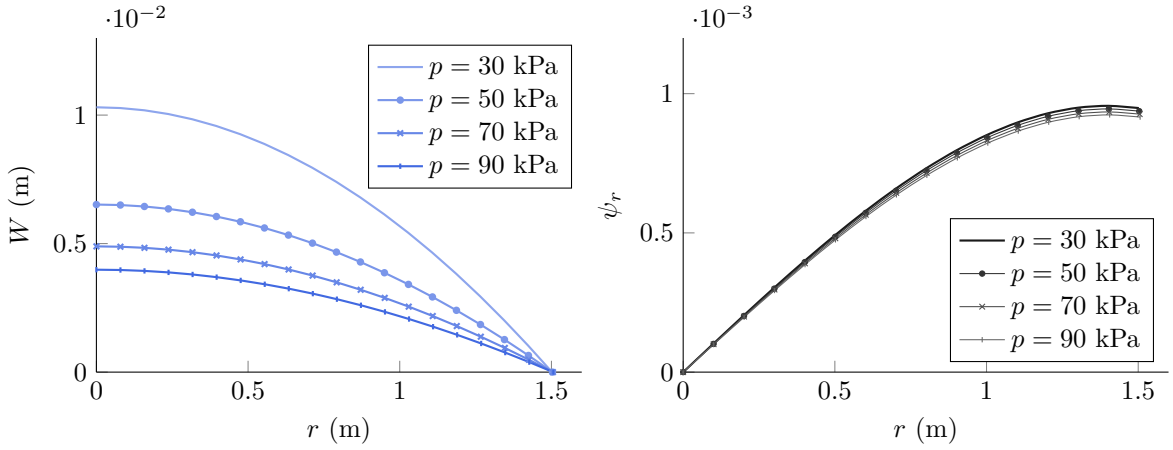

(b) $H_\varnothing = 20$ cm

Figure 10: Deflection W and fiber rotation ψ_r for a simply supported circular panel subjected to uniform vertical load $q = 100$ Pa for four different inflation pressures p ($R_\varnothing = 1.5$ m).

depends on the pressure p via coefficients K and K' and also via (R, H) given by Relations (44)–(45). However, the numerical computations show that the dependence of ψ_r on p is rather weak, see Fig. 10. The values of the rotation ψ_r are very small (here 10^{-3}), which means that the fibers remain practically vertical during the deformation process.

In order to show the sensitivity of the deflection W to the value of the membrane Young modulus E, use is made again of solution (51) to compute W with two values different by ± 0.8 GPa from $E = 2.5$ GPa, namely $E = 1.7$ GPa and $E = 3.3$ GPa. It is observed that W varies monotonically with E, so that two curves are enough to draw the envelope. Moreover, as one can see in Fig. 11, the larger the external load q is, the greater the influence of E on

the deflection.

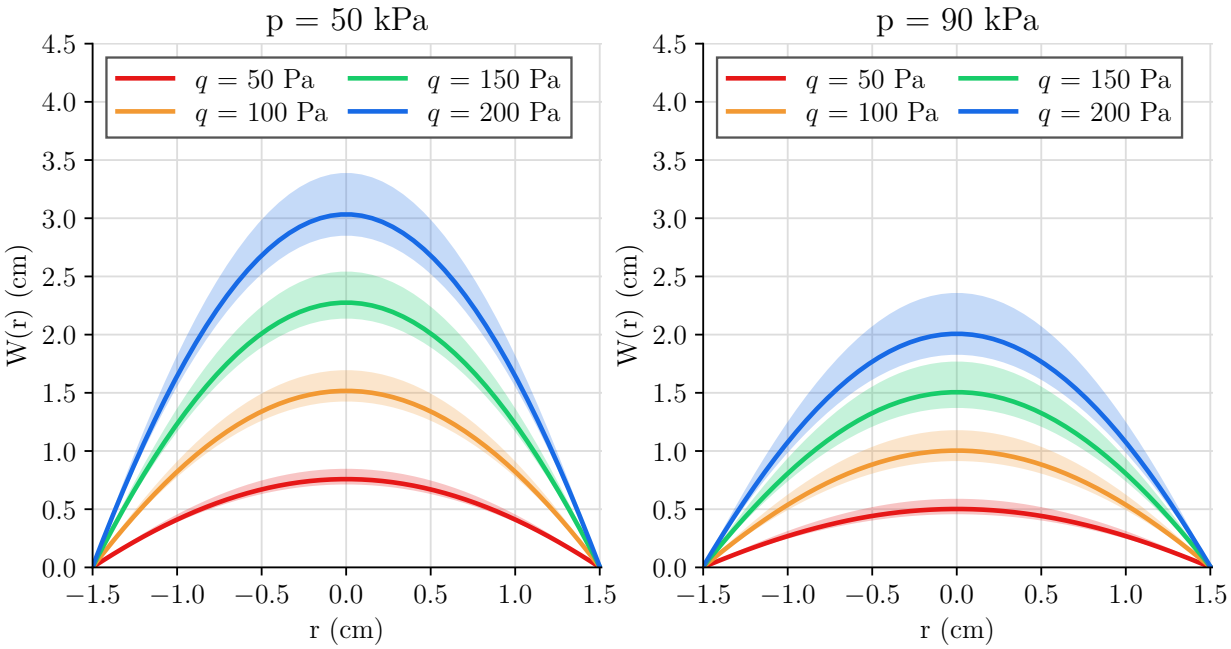

Figure 11: Sensitivity of the deflection to the membrane's Young modulus E for two inflation pressures and four external loads ($R_\varnothing = 1.5$ m, $H_\varnothing = 10$ cm, $E = 2.5$ GPa for the thick line).

5.3. Limit of validity of the solution – Wrinkling load

While fabric materials can withstand large tensile stresses, their stiffness when subjected to compressive stress is very low. Large deformations may cause the net stress to become zero or negative, giving rise to a localized buckling phenomenon, commonly named wrinkling. Upon finding a solution, one must check that the stresses are positive everywhere in the membranes for the analytical solution to remain valid. The load for which the stress becomes zero is called the wrinkling load q_w.

Let us compute the strain tensors at every point of the panel. Inserting the solution (51) into Relation (29) gives

$$\mathrm{Mat}(\boldsymbol{E};\boldsymbol{e}_r\boldsymbol{e}_\theta\boldsymbol{e}_3) = Z\begin{bmatrix}\psi_{r,r} & 0\\ 0 & \frac{\psi_r}{r}\end{bmatrix} = \frac{Zq}{16K}\begin{bmatrix}\frac{3K+K'}{K+K'}R^2-3r^2 & 0\\ 0 & \frac{3K+K'}{K+K'}R^2-r^2\end{bmatrix} \tag{52}$$

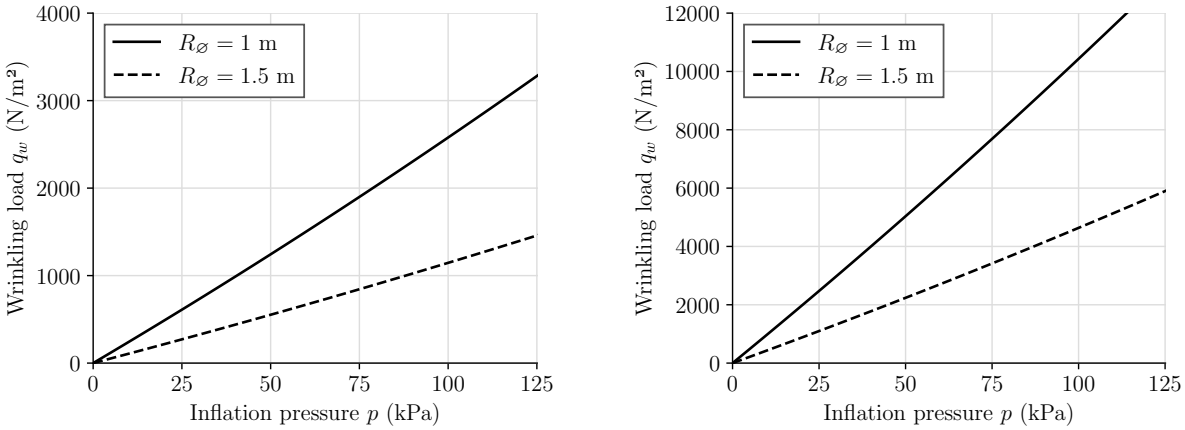

(a) Panel height $H_\varnothing = 10$ cm.

(b) Panel height $H_\varnothing = 20$ cm.

Figure 12: Wrinkling load of the bending solution for two different panel radii and heights.

The reduced constitutive law (31) yields the principal stresses:

$$\Sigma^{rr} = \frac{p\tilde{H}}{2\tau} + \frac{EZq}{16K(1-\nu^2)}\left(\frac{3K+K'}{K+K'}R^2(1+\nu) - r^2(3+\nu)\right)$$
$$\Sigma^{\theta\theta} = \frac{p\tilde{H}}{2\tau} + \frac{EZq}{16K(1-\nu)}\left(\frac{3K+K'}{K+K'}R^2 - r^2\right)$$

The principal stresses reach their maximum for $r = 0$ and $Z = \pm H/2$ (depending on the sign of q). Canceling either Σ^{rr} or $\Sigma^{\theta\theta}$ gives the same expression of the wrinkling load:

$$q_w = \pm\frac{p\tilde{H}}{\tau H}\frac{16K(1-\nu)}{ER^2\frac{3K+K'}{K+K'}} \tag{53}$$

The coefficients K and K' are combinations of the membrane flexural rigidity and the pre-stress caused by inflation. For small pressures and small panel heights, the pre-stress term is very small compared to the flexural rigidity term, so that $K \approx \dfrac{E\tilde{\tau}H^2}{2(1-\nu^2)}$ and $K' \approx \nu K$. Consequently, the wrinkling load is almost a linear function of the inflating pressure, see Fig. 12. Note that the so-called wrinkling load q_w is only an estimation based on the linearized theory: it cannot predict the actual onset of wrinkling for strongly nonlinear problems.

6. Comparison between the analytical solution and a 3D finite element solution

To conclude this study of inflatable panels, we shall compare the above analytical results for a circular panel with 3D nonlinear finite element simulations. The finite element solution is obtained using an in-house membrane code which exploits Ken Brakke's Surface Evolver program [25] and is based on a finite strain and large displacement formulation. The 3D structure comprises three membranes (upper, lower and lateral) and drop cords that connect the upper and lower faces. The initial mesh has an overall thickness $H_\varnothing$ and a radius $R_\varnothing$. The values of $H_\varnothing$, $R_\varnothing$, τ, E and ν are the same as in Table 1. The membranes are discretized using 3-node pure membrane triangular elements and the yarns as 2-node bar elements connecting the upper and lower surfaces, Fig. 13. The mesh is created from a simple geometry which is then subdivided until the best trade-off between accuracy and computational time is reached at a total of 3072 facets. Special care must be taken to account for the overall yarns stiffness without modeling them individually, and their high rigidity can pose numerical challenges, making the simulation of inflatable panels a difficult task. Boundary conditions are applied so as to prevent rigid body motions: $U_x(X = 0) = 0$ and $U_y(Y = 0) = 0$. The inflatable panel is subjected to various inflation pressures p as mentioned in Table 3. After the panel is pressurized at a pressure p, the natural radius $R_\varnothing$ becomes R and the natural height $H_\varnothing$ becomes H; both reference dimensions R and H of the panel are used in Eq. (51). Once the structure is inflated, a vertical dead load q is applied. Half of this external load is applied to the top membrane and the other half to the bottom membrane.

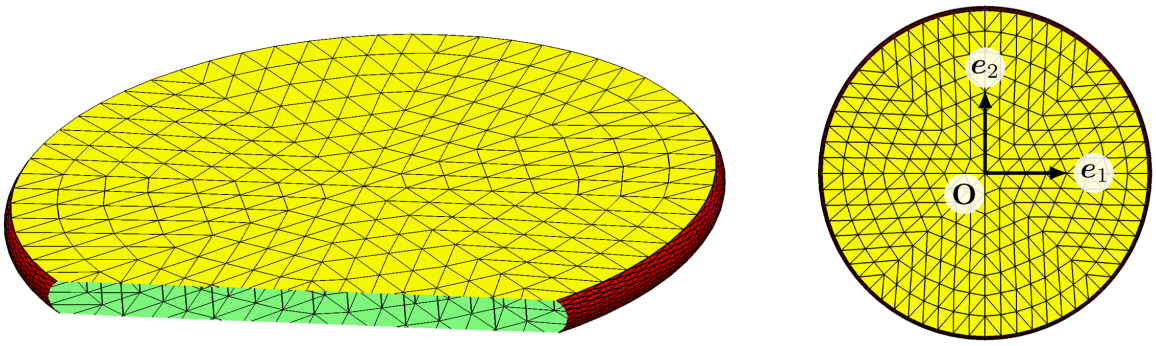

Figure 13: Cut-view and top view of the mesh used in the simulations in the reference configuration.

The finite element model takes into account all nonlinearities for the membranes and yarns, as well as the follower effect of the pressure that remains normal to the membrane.

The gas used for inflation is taken into account exclusively through the pressure load it generates and does not constitute a heavy material medium, as justified by the static nature of the study. The finite element solutions are found by minimizing the total potential energy with respect to the current nodal position, using the conjugate gradient method. At every load increment the program goes through several iterations, updating the position of the nodes until convergence is reached, that is, when the energy step size becomes smaller than a given threshold of 10^{-8} J. In some cases, convergence is hard to reach due to numerical instabilities. When this occurs, certain nodes are artificially displaced by a very small amount to escape from local energy minima. Fig. 14 shows the maximal deflection $W(r=0)$ as a function of the external load q for two different geometries and two inflation pressures $p = 50$ kPa and $p = 90$ kPa. The analytical solution is only plotted for external load q less than the wrinkling load q_w defined by Relation (53). Recall that the linear elastic solution for the inflatable panel is valid as long as (i) the displacements and rotations are small (see Subsection 4.1) and (ii) the load q is less than the wrinkling load q_w given by (53). Criterion (i) may be expressed in terms of ratio $W(r=0)/R_\varnothing$ and $\psi_r(r=0)$ for instance, say $W(r=0)/R_\varnothing < 3\%$ and $\psi_r(r=0) < 1\%$. The present results show that the higher the inflating pressure p and the membrane thickness $H_\varnothing$ are, the larger the range of validity of the solution – defined by the above-mentioned criteria (i) and (ii) – and the larger the external load q, or equivalently, the higher the bearing capacity of the panel. Furthermore, it can be seen in Fig. 14 that the criterion $W(r=0)/R_\varnothing < 3\%$ may be violated before criterion $q < q_w$. In other words, one can go beyond the linear elastic range before reaching the wrinkling load.

The analytical maximum deflection, denoted W_{theor}, and the maximum deflection given by the 3D finite element computations, denoted W_{FE}, are given in Table 3 for a uniform vertical load $q = 100$ Pa. The relative difference is defined as $(W_{\text{FE}} - W_{\text{theor}})/W_{\text{theor}}$.

The comparison between W_{theor} and W_{FE} can be conducted in terms of the ratio $H_\varnothing/R_\varnothing$ and the external load q, respectively:

– Table 3 shows that, as expected, at a given pressure p, the smaller the ratio $H_\varnothing/R_\varnothing$ is, the better the panel analytical solution compares with the 3D finite element computations.

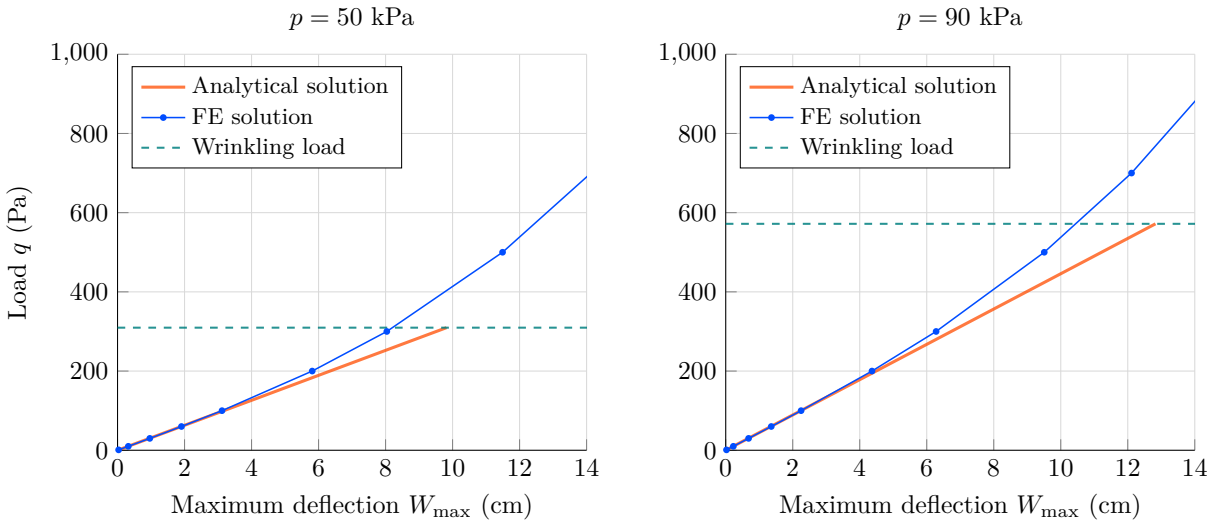

(a) $R_\varnothing = 2$ m, $H_\varnothing = 10$ cm

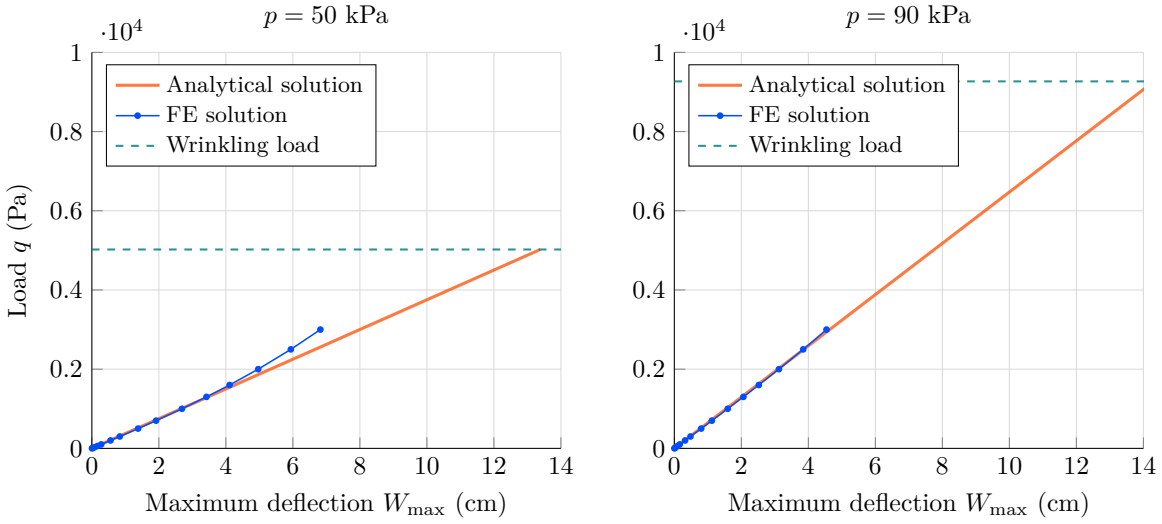

(b) $R_\varnothing = 1$ m, $H_\varnothing = 20$ cm

Figure 14: Linearized analytical load-deflection curves compared with the finite element results for two different geometries and inflation pressures. The analytical curves stop when the assumption of positive tensile stress is no longer valid ($q > q_w$).

– For a given geometry and pressure p, the deflection varies with the external load q ranging from 0 to 800 Pa as shown in Fig. 14. In the range where the load q is small enough for the linear solution to be valid, the analytical solution and the finite element results are found to be in fairly good agreement.

So far, all the numerical computations have been made with the membrane Young mod-

p (kPa)	$H_\varnothing$ (cm)	H (cm)	$R_\varnothing$ (m)	R (m)	W_{FE} (mm)	W_{theor} (mm)	Relative difference (%)	Wrinkling load q_w (Pa)
30	10	10.10	1.0	1.001	9.32	9.11	2.2	734
			1.5	1.501	22.28	22.59	-1.4	326
			2.0	2.002	42.68	45.37	-5.9	183
	20	20.20	1.0	1.001	4.61	4.34	6.1	2975
			1.5	1.502	10.71	10.30	4.0	1321
			2.0	2.003	20.14	19.60	2.8	743
50	10	10.17	1.0	1.001	5.88	5.73	2.7	1239
			1.5	1.502	15.07	14.95	0.8	550
			2.0	2.002	31.18	31.71	-1.7	310
	20	20.33	1.0	1.002	2.79	2.66	4.5	5022
			1.5	1.503	6.76	6.52	3.8	2230
			2.0	2.004	13.28	12.86	3.2	1254
70	10	10.23	1.0	1.001	4.38	4.27	2.7	1757
			1.5	1.502	11.81	11.65	1.4	781
			2.0	2.003	25.72	25.78	-0.3	439
	20	20.47	1.0	1.002	2.02	1.95	4.1	7119
			1.5	1.504	5.08	4.89	3.8	3161
			2.0	2.006	10.28	9.96	3.2	1778
90	10	10.30	1.0	1.002	3.55	3.46	2.7	2288
			1.5	1.503	9.96	9.80	1.7	1017
			2.0	2.004	22.50	22.43	0.3	572
	20	20.60	1.0	1.003	1.61	1.54	3.9	9267
			1.5	1.506	4.14	3.98	3.9	4115
			2.0	2.008	8.62	8.33	3.4	2314

Table 3: Analytical and 3D finite element results for a simply supported circular inflatable panel ($q = 100$ Pa, $E = 2.5$ GPa).

ulus $E = 2.5$ GPa. In order to show the sensitivity of the deflections to the value of E, we conduct a new series of computations taking now $E = 0.59$ GPa and the same values for all other quantities. This new value of E, significantly smaller than the previous one, was measured on an inflatable panel that will be used in our experiments.

Table 4, similar to Table 3, displays the results corresponding to $E = 0.59$ GPa. These additional numerical values confirm that the inflated height H is insensitive to the membrane's Young modulus. Here again, the values given by the inflatable panel theory agree quite well with those from the 3D finite element computations. Overall, the largest discrep-

ancy between the theory and the finite element computations occurs at radius $R_\varnothing = 2$ m and height $H_\varnothing = 10$ cm, which is the geometry corresponding to the lowest wrinkling load as can be seen in the last column of Table 4. The relative difference is negative, meaning that the analytical solution overestimates the deflection.

p (kPa)	$H_\varnothing$ (cm)	H (cm)	$R_\varnothing$ (m)	R (m)	W_{FE} (mm)	W_{theor} (mm)	Relative difference (%)	Wrinkling load q_w (Pa)
30	10	10.10	1.0	1.003	11.80	11.57	2.0	732
			1.5	1.504	34.52	34.94	-1.2	325
			2.0	2.006	76.64	84.25	-9.0	183
	20	20.20	1.0	1.005	5.21	4.99	4.5	2965
			1.5	1.509	13.98	13.46	3.8	1316
			2.0	2.012	30.33	29.47	2.9	741
50	10	10.17	1.0	1.005	8.38	8.17	2.6	1235
			1.5	1.507	27.28	27.21	0.3	549
			2.0	2.010	66.22	70.34	-5.9	309
	20	20.33	1.0	1.010	3.48	3.31	5.0	4991
			1.5	1.515	10.10	9.68	4.4	2217
			2.0	2.019	23.45	22.73	3.2	1247
70	10	10.23	1.0	1.007	6.89	6.70	2.8	1750
			1.5	1.510	23.93	23.83	0.4	778
		10.24	2.0	2.014	60.84	64.15	-5.2	438
	20	20.47	1.0	1.014	2.74	2.59	5.5	7056
			1.5	1.521	8.41	8.05	4.5	3136
			2.0	2.028	20.35	19.83	2.6	1764
90	10	10.30	1.0	1.009	6.04	5.87	2.9	2276
			1.5	1.513	21.92	21.90	0.1	1012
			2.0	2.018	57.51	60.54	-5.0	569
	20	20.60	1.0	1.018	2.32	2.19	5.8	9163
			1.5	1.527	7.44	7.14	4.2	4073
			2.0	2.036	18.52	18.20	1.8	2291

Table 4: Analytical and 3D finite element results for a simply supported circular inflatable panel with a smaller elastic modulus ($q = 100$ Pa, $E = 0.59$ GPa).

Some final remarks can be made regarding the modified dimensions $\tilde{\tau}$ and $\tilde{H}$ introduced in subsections 3.5–3.6. When making the approximation $\tilde{\tau} \approx \tau$ the relative difference will generally not deteriorate unless the membranes are particularly thick or the panel is very thin. On the other hand, considering H instead of $\tilde{H} = H - 2\tau$ in (51) worsens the results

as it increases the relative difference by up to 2 percentage points on every test case. This is mostly due to the fact that $\tilde{H}$ is squared or cubed in several expressions, notably in the coefficients K and K'.

7. Conclusion

In this work, it has been shown that the principle of virtual power, when combined with the Reissner-Mindlin kinematics and the membrane model, is an efficient tool to obtain the governing equations for inflatable panels. The nonlinear equations (24)–(26), established in the context of finite deformation, and the subsequent linearized equations (37)–(43), all contain the essential terms due to the inflating pressure, necessary for correctly accounting for the load-bearing capacity of inflatable panels.

Solving the linearized equations has given rise to the analytical solution (51) for the static bending problem of a uniformly loaded inflatable disk undergoing static bending, together with Relation (53) providing the limit of validity related to the wrinkling of the membranes. The numerical results obtained from the analytical solution have been found to be in good agreement with those obtained from a 3D finite element program.

Future works will include utilizing the linearized equations to investigate the vibrations and the buckling of inflatable panels, as well as the experimental validation of the theoretical model proposed herein.

References

[1] SaP-Report: Prospect for European guidance for the Structural Design of Tensile Membrane Structures. Science and Policy Report. Publications Office of the European Union, Luxembourg, 2016.

[2] R. L. Comer, S. Levy, Deflections of an inflated circular-cylindrical cantilever beam, AIAA Journal 1 (7) (1963) 1652–1655.

[3] J. P. H. Webber, Deflections of inflated cylindrical cantilever beams subjected to bending and torsion, The Aeronautical Journal 86 (858) (1982) 306–312.

[4] J. A. Main, S. W. Peterson, A. M. Strauss, Load-deflection behavior of space-based inflatable fabric beams, Journal of Aerospace Engineering 7 (2) (1994) 225–238.

[5] J. A. Main, S. W. Peterson, A. M. Strauss, Beam-type bending of space-based inflated membrane structures, Journal of Aerospace Engineering 8 (2) (1995) 120–125.

[6] W. B. Fichter, A theory for inflated thin-wall cylindrical beams, NASA Technical Note D-3466, NASA Scientific and technical publications (Jun. 1966).

[7] E. C. Steeves, A linear analysis of the deformation of pressure stabilized beams, NASA Technical Report 75-47-AMEL, US Army Natick Laboratories (Jan. 1975).

[8] C. Wielgosz, J.-C. Thomas, Deflections of inflatable fabric panels at high pressure, Thin-Walled Structures 40 (6) (2002) 523–536.

[9] A. Le van, C. Wielgosz, Bending and buckling of inflatable beams: some new theoretical results, Thin-Walled Structures 43 (8) (2005) 1166–1187.

[10] K. L. Apedo, S. Ronel, E. Jacquelin, M. Massenzio, A. Bennani, Theoretical analysis of inflatable beams made from orthotropic fabric, Thin-Walled Structures 47 (2009) 1507–1522.

[11] T. T. Nguyen, S. Ronel, M. Massenzio, K. L. Apedo, E. Jacquelin, Analytical buckling analysis of an inflatable beam made of orthotropic technical textiles, Thin-Walled Structures 51(0) (2012) 186–200.

[12] T. T. Nguyen, S. Ronel, M. Massenzio, E. Jacquelin, K. L. Apedo, Huan Phan-Dinh, Numerical buckling analysis of an inflatable beam made of orthotropic technical textiles, Thin-Walled Structures 72 (2013) 61–75.

[13] Q. T. Nguyen, J.-C. Thomas, A. Le van, Inflation and bending of an orthotropic inflatable beam, Thin-Walled Structures 88 (2015) 129–144.

[14] R. W. Leonard, G. W. Brooks, H. G. McComb, Structural Considerations of Inflatable Reentry Vehicles, NASA Technical Note D-457, NASA (Sep. 1960).

[15] H. G. McComb, A linear theory for inflatable plates of arbitrary shape, NASA Technical Note D-930, NASA (Oct. 1961).

[16] L. M. Habip, A review: Recent work on inflatable structures, International Journal of Mechanical Sciences 7 (2) (1965) 149–152.

[17] P. Cavallaro, C. Hart, A. Sadegh, Mechanics of air-inflated drop-stitch fabric panels subject to bending loads, Vol. 9, 2013.

[18] C. Wielgosz, J.-C. Thomas, An inflatable fabric beam finite element, Communications in Numerical Methods in Engineering 19 (4) (2003) 307–312.

[19] M. Kawabata, K. Ishii, Effective stiffness evaluation of air-inflated dual membrane plates consist of drop cords and curved covers due to internal pressure (in Japanese), Journal of Structural and Construction Engineering (Transactions of AIJ) 62 (1997) 61–67.

[20] M. Smith, Mechanical response of polymer-fabric skin materials used in inflatable drop-stitch structures (Master Thesis), University of Rhode Island, 2019.

[21] A. Alich, Modeling, simulation and investigation of inflatable drop-stitch panels with finite element analysis (Master Thesis), University of Rhode Island, 2019.

[22] R. Buglio, Characterization of drop-stitch constituent materials and inflated panel response (Master Thesis), University of Rhode Island, 2020.

[23] W. G. Davids, H. Zhang, Beam finite element for nonlinear analysis of pressurized fabric beam-columns, Engineering Structures 30 (2008) 1969–1980.

[24] W. G. Davids, E. Waugh, S. Vel, Experimental and computational assessment of the bending behavior of inflatable drop-stitch fabric panels, Thin-Walled Structures 167 (2021) 108178.

[25] K. A. Brakke, The Surface Evolver, Experimental Mathematics 1 (2) (1992) 141–165.